*J. Fluid Mech.* (1985), *vol.* 155, *pp.* 233–265
*Printed in Great Britain*



# Source–sink flow inside a rotating cylindrical cavity

By J. M. OWEN, J. R. PINCOMBE AND R. H. ROGERS
School of Engineering and Applied Sciences, University of Sussex

(Received 18 May 1984 and in revised form 17 December 1984)

The axisymmetric flow inside a rotating cavity with radial outflow or inflow of fluid is discussed. The basic theoretical model of Hide (1968) is extended, using the integral-momentum techniques of von Kármán (1921), to include laminar and turbulent flows; both linear and nonlinear equations are considered. The size of the source region is estimated using a 'free disk' model for the outflow case and a free vortex for the inflow case. In both cases, the estimates are in good agreement with available experimental data. Theoretical values of the tangential component of the velocity outside the Ekman layers on the disks, obtained from solutions of the laminar and turbulent integral equations, are compared with experimental values. The experiments were conducted in a number of rotating-cavity rigs, with a radial outflow or inflow of air, and laser-Doppler anemometry was used to measure the velocity in the 'interior core' between the Ekman layers. The measurements provide good support for the theoretical models over a wide range of flow rates, rotational speeds and radial locations. Although only isothermal flow is considered in this paper, the methods can be readily extended to non-isothermal flow and heat transfer.

## 1. Introduction

A problem of great importance to the gas-turbine designer is the heat transfer resulting from the flow of the air inside the cavity between corotating turbine or compressor disks. In some cases these rotating cavities are sealed at their inner and outer radii; in other cases they may be open to allow either radial inflow or radial outflow of cooling air. Such flows are, in the practical cases, usually turbulent and buoyancy effects are often significant.

In this paper, an idealized model of these flows is represented by the cylindrical cavity shown in figure 1. This cavity has axial width $s$, inner radius $a$ and outer radius $b$, and is rotating with angular speed $\Omega$. There may be a radial outflow of fluid, with a volume flow rate $Q$, from a source at the cylindrical surface of radius $a$ to a sink at the cylindrical surface of radius $b$; alternatively, there may be a radial inflow, in which the positions of the source and the sink are reversed. The flow structures for both inflow and outflow are shown schematically in the figure, and will be described in greater detail in §4.

Isothermal laminar flow in such a cavity has been studied analytically by Hide (1968), Barcilon (1970) and Bennetts & Hocking (1973), and numerically by Bennetts & Jackson (1974) and by Chew, Owen & Pincombe (1984). Such flows are often described in terms of a Rossby number ($Ro = \bar{v}/2\Omega s$, where $\bar{v}$ is the tangential component of velocity in the interior core) and an Ekman number ($Ek = \nu/\Omega s^2$, where $\nu$ is the kinematic viscosity). For small values of these non-dimensional parameters (more precisely, for $Ro \ll Ek^{\frac{1}{2}} \ll 1$) the inertial terms in the boundary-layer equations, referred to a rotating frame of reference, can be neglected to produce linear equations

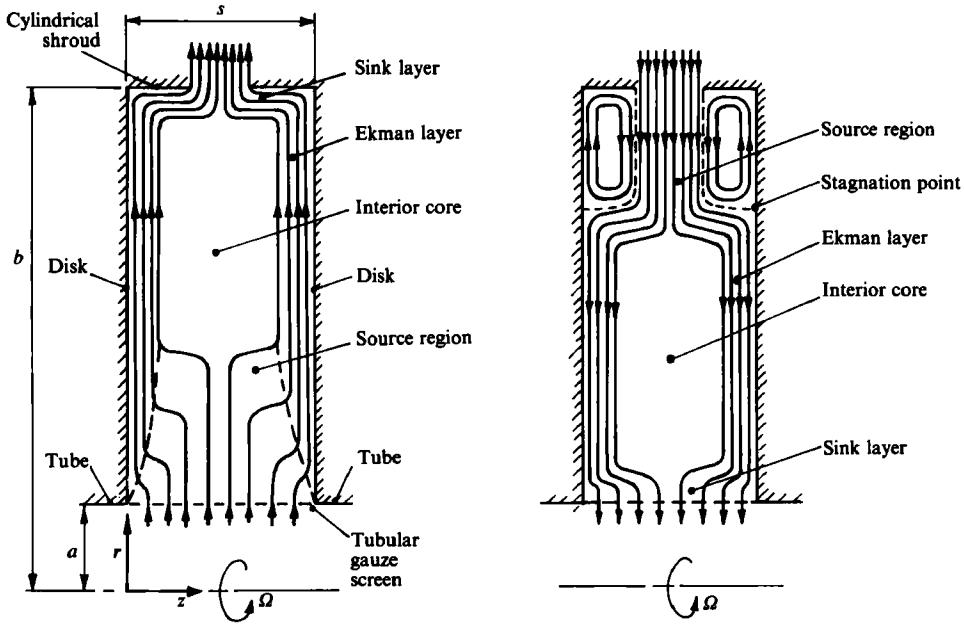


FIGURE 1. Schematic diagram of source–sink flow in a rotating cavity.

which can easily be solved; for this case, each Ekman layer has a thickness of order $Ek^{\frac{1}{2}}$.

Whilst the laminar-flow case has been studied extensively, little information is available about turbulent source–sink flow. Ekman-layer instabilities were studied by Faller (1963) and by Tatro & Mollo-Christensen (1967) for the case of radial inflow. They observed two types of long-wavelength cellular disturbance for $Re_r \gtrsim 56$ (where $Re_r = |Q|/2\pi\nu r$). For values of $Re_r \gtrsim 125$, the first manifestations of turbulence were observed as bursts of high-frequency fluctuations superimposed on a low-frequency periodic structure. Similar effects were observed by Owen & Pincombe (1980*a*) for radial outflow; they also noted that the measured values of the tangential component of velocity in the interior core departed from the theoretical linear laminar value for $Re_r$ greater than about 200.

For gas-turbine and compressor disks, it is to be expected that the heat transfer is strongly controlled by the flow inside the Ekman layers; it is, therefore, useful to investigate these flows in some detail. In this paper, the discussion will be limited to the consideration of isothermal flows in which the effect of buoyancy on the flow is neglected. The extension of the theoretical work presented here to the more general case is straightforward and, currently, comparison of the extended theory with the data from heat-transfer experiments is in progress. It is hoped to report on this work in the near future.

In order to calculate the flow in a cavity, integral-momentum techniques are used; these have the advantage of comparative simplicity and ease of solution for turbulent as well as for laminar flow. The integral equations have been used extensively for rotating flows relative to inertial frames of reference (see Greenspan 1968). In a rotating frame, however, the equations can be linearized to provide simple analytical solutions to the complicated problem of source–sink flows in rotating cavities.

In §2 of this paper, a short summary is given of the (linear) theory of Hide (1968)

for laminar flow and of the use by von Kármán (1921) of integral-momentum equations to determine the turbulent flow over a 'free disk' rotating in an otherwise quiescent fluid. The integral-momentum technique is then used to extend Hide's work to the turbulent case. Since the theory is to be compared with experimental data, much of which has not been published elsewhere, §3 contains a brief description of the apparatus used in the experiments, and of the measuring techniques involved. The structure of the flow, together with estimates of the size of the region near the source, is discussed in §4, both for radial outflow and for radial inflow. In §5, the integral-momentum technique is applied to the full boundary-layer equations, referred to a rotating frame, in order to predict the thickness of the Ekman layers and the tangential component of velocity in the core. The velocity predictions are compared with the data obtained in the experiments in §6, and a summary of the conclusions is given in §7.

## 2. Ekman layers and 'free disk' theory

The theoretical work presented in this paper is largely an extension and combination of the (linear) theory of Hide (1968) and the (integral-momentum) theory of von Kármán (1921). It is useful to give a brief summary of their work at this stage before developing the main theme of this paper. The notation used here is not necessarily that used by the original authors, and it is convenient to summarize the present notation here.

As shown in figure 1 (*a*), the cavity is rotating about the $z$-axis with angular speed $\Omega$; the disks lie in the planes $z = 0$ and $z = s$ and most of the discussion here is related to the boundary layer on the disk for which $z = 0$. The cavity is bounded on the outside by a perforated shroud at $r = b$ (where $r$ is the distance from the axis of rotation). There is a central hole of radius $a$ in one (or both) of the disks, through which fluid is introduced into, or extracted from, the cavity. Cylindrical polar coordinates $(r, \phi, z)$ are used and the corresponding velocity is $(u, v_\phi, w)$ referred to a stationary frame of reference and $(u, v, w)$ referred to a frame of reference rotating with the cavity: clearly $v_\phi = v + \Omega r$. The shear stress within the boundary layer has components $\tau_r, \tau_\phi$ in the radial and tangential directions respectively; the pressure (which, as is usual in boundary-layer theory, is independent of $z$ within the boundary layer) is denoted by $\bar{p}$. Overbars are used throughout to indicate values outside the boundary layers on the disks, and the subscript zero is used for values on the disk $z = 0$.

The volume flow rate of the fluid entering the cavity is $Q$; $Q$ is taken to be positive if the flow is outwards and negative if the flow is inwards. The local volume flow rate through one of the boundary layers on the disks at a radius $r$ is denoted by $Q_1$. The density of the fluid is $\rho$, its dynamic viscosity is $\mu$ (the kinematic viscosity being $\nu = \mu/\rho$); for isothermal flow, these quantities are assumed to remain constant.

There are two non-dimensional parameters which are used extensively: these are the volume flow-rate coefficient

$$C_w = Q/\nu b, \tag{2.1}$$

and the rotational Reynolds number

$$Re_\phi = \Omega b^2/\nu. \tag{2.2}$$

It may be noted that $Re_\phi$ is the reciprocal of the Ekman number defined in the Introduction. In addition, it is occasionally useful to use the radial Reynolds number

$$Re_r = |Q|/2\pi\nu r. \tag{2.3}$$

### 2.1. *The Ekman layers in laminar flow*

For incompressible, laminar flow in which Coriolis forces dominate over inertial and centrifugal forces, Ekman layers (see, for example, Greenspan 1968) form on the disks. Outside the Ekman layers, there is a balance between the Coriolis and the pressure forces so that, in a frame of reference rotating with the cavity,

$$-2\Omega\bar{v} = -\frac{1}{\rho}\frac{\partial\bar{p}}{\partial r}, \quad 2\Omega\bar{u} = -\frac{1}{\rho r}\frac{\partial\bar{p}}{\partial\phi}. \tag{2.4}$$

From these equations, together with the equation of continuity

$$\frac{\partial(r\bar{u})}{\partial r}+\frac{\partial\bar{v}}{\partial\phi}+r\frac{\partial\bar{w}}{\partial z} = 0,$$

it is clear that $\partial\bar{w}/\partial z = 0$ (this is also a consequence of the Taylor–Proudman theorem). For the isothermal rotating cavity, it is reasonable to assume that there is symmetry about the mid-axial plane $z = \frac{1}{2}s$; it follows that, in the region between the Ekman layers in the cavity, $\bar{w} = 0$ and the Ekman layers are non-entraining. This is a special case of the result first proved by Hide (1968), and it true both for laminar and for turbulent incompressible flow; it is not necessarily true for flows which are not symmetrical about the mid-axial plane.

Within the Ekman layers viscous forces are also important; after the usual boundary-layer approximations are made, it is found that, for laminar flow,

$$-2\Omega(v-\bar{v}) = \nu\frac{\partial^2 u}{\partial z^2}, \quad 2\Omega(u-\bar{u}) = \nu\frac{\partial^2 v}{\partial z^2}. \tag{2.5}$$

The corresponding boundary conditions are

$$\left.\begin{aligned} &u = v = 0 \quad \text{when } z = 0,\\ &u\to\bar{u}, \quad v\to\bar{v} \quad \text{as } z\to\infty. \end{aligned}\right\} \tag{2.6}$$

As long as the flow is axisymmetric, it is clear from the second of (2.4) that $\bar{u} = 0$; it is worth noting that this is true also for turbulent flow and for flows where buoyancy is important.

The solution of (2.5), subject to the conditions (2.6), is (when $\bar{u} = 0$):

$$u = -\bar{v}\,\mathrm{e}^{-z/D}\sin\frac{z}{D}, \quad v = \bar{v}\left[1-\mathrm{e}^{-z/D}\cos\frac{z}{D}\right], \tag{2.7}$$

where

$$D = \left(\frac{\nu}{\Omega}\right)^{\frac{1}{2}} = Re_\phi^{-\frac{1}{2}}b. \tag{2.8}$$

The local value of the volume flow rate is

$$Q_1 = \int_0^\infty 2\pi r u\,\mathrm{d}z, \tag{2.9}$$

and, using (2.7), this gives

$$\frac{Q_1}{\nu b} = -\pi\,Re_\phi^{\frac{1}{2}}\frac{\bar{v}}{\Omega r}\left(\frac{r}{b}\right)^2. \tag{2.10}$$

If the incoming fluid is equally divided between the two Ekman layers in the cavity, so that $Q_1 = \frac{1}{2}Q$, it follows from (2.10) that

$$\frac{\bar{v}}{\Omega r} = -\frac{1}{2\pi}C_w\,Re_\phi^{-\frac{1}{2}}\left(\frac{r}{b}\right)^{-2}. \tag{2.11}$$

For isothermal turbulent flow, it is possible to find a solution to the equations corresponding to (2.5) if a mixing-length theory is used for the Reynolds stresses, but there appears to be no simple expression such as (2.11) relating $\bar{v}$ to $C_w$ and $Re_\phi$.

### 2.2. *The free disk*

The flow due to a disk rotating in free space was first discussed by von Kármán (1921). The equations valid in the boundary layer on the disk (at $z = 0$) are, in a stationary frame of reference,

$$\left.\begin{aligned} \frac{1}{r}\frac{\partial}{\partial r}(ru)+\frac{\partial w}{\partial z} &= 0, \\ u\frac{\partial u}{\partial r}+w\frac{\partial u}{\partial z}-\frac{v_\phi^2}{r} &= \frac{1}{\rho}\frac{\partial \tau_r}{\partial z}, \\ u\frac{\partial v_\phi}{\partial r}+w\frac{\partial v_\phi}{\partial z}+\frac{uv_\phi}{r} &= \frac{1}{\rho}\frac{\partial \tau_\phi}{\partial z}, \end{aligned}\right\} \tag{2.12}$$

and the boundary conditions are

$$\left.\begin{aligned} u = 0, \quad v_\phi = \Omega r, \quad w = 0 \quad \text{when } z = 0, \\ u \to 0, \quad v \to 0 \quad \text{when } z \to \infty. \end{aligned}\right\} \tag{2.13}$$

Cochran (1934) found a similarity solution for this system in the laminar case. His work will not be discussed here, but it is useful to quote the values he obtained for $Q_1$ and for the 'thickness', $\delta^*$, of the boundary layer, outside of which the tangential component of velocity is effectively zero. These are given by

$$\frac{Q_1}{\nu b} = 0.886\pi\, Re_\phi^{\frac{1}{2}}\left(\frac{r}{b}\right)^2, \quad \frac{\delta^*}{b} \approx 5\, Re_\phi^{-\frac{1}{2}}. \tag{2.14}$$

For the turbulent case, von Kármán used an integral momentum method; he assumed that, in the boundary layer,

$$u = \begin{cases} u_1(r)\left(\dfrac{z}{\delta^*}\right)^{\frac{1}{7}}\left(1-\dfrac{z}{\delta^*}\right), & z \leqslant \delta^*, \\ 0, & z > \delta^*, \end{cases} \tag{2.15}$$

$$v_\phi = \begin{cases} \Omega r\left[1-\left(\dfrac{z}{\delta^*}\right)^{\frac{1}{7}}\right], & z \leqslant \delta^*, \\ 0, & z > \delta^*, \end{cases} \tag{2.16}$$

where $u_1$ and $\delta^*$ are functions of $r$ to be determined. Equations (2.12) are integrated with respect to $z$ from 0 to $\infty$, $w$ being eliminated and the expressions in (2.15) and (2.16) used for $u$ and $v_\phi$. This gives expressions for $\tau_{r,0}$ and $\tau_{\phi,0}$, the values of $\tau_r$ and $\tau_\phi$ respectively when $z = 0$.

It is assumed that, for $z/\delta^* \ll 1$,

$$\frac{\tau_r}{\tau_\phi} = \frac{u}{v_\phi - \Omega r}, \tag{2.17}$$

and (by analogy with flow in a pipe)

$$\frac{q}{q_*} = \left(\frac{q_* z}{\nu}\right)^{\frac{1}{4}}, \tag{2.18}$$

where $$q = [u^2+(v_\phi-\Omega r)^2]^{\frac{1}{2}}, \quad q_*^2 = \frac{(\tau_r^2+\tau_\phi^2)^{\frac{1}{2}}}{\rho}.$$

After some manipulation, this gives

$$\left.\begin{aligned}\frac{\tau_{r,0}}{\rho} &= 0.0225\left(\frac{\nu}{\delta^*}\right)^{\frac{1}{4}} u_1(u_1^2+\Omega^2r^2)^{\frac{3}{8}},\\ \frac{\tau_{\phi,0}}{\rho} &= -0.0225\left(\frac{\nu}{\delta^*}\right)^{\frac{1}{4}} \Omega r(u_1^2+\Omega^2r^2)^{\frac{3}{8}},\end{aligned}\right\} \tag{2.19}$$

and these expressions are substituted into the integrated equations of motion. This results in two ordinary differential equations for the unknown quantities $u_1$ and $\delta^*$.

The solution given by von Kármán for these equations is

$$\frac{u_1}{\Omega r} = 0.162, \quad \frac{\delta^*}{b} = 0.525\, Re_\phi^{-\frac{1}{5}}\left(\frac{r}{b}\right)^{\frac{3}{5}}, \tag{2.20}$$

and it is possible to show that, for any initial conditions (at $r = 0$), the solution rapidly converges to that given by (2.20). The value of $Q_1$ (using (2.9)) is then given by

$$\frac{Q_1}{\nu b} = 0.219\, Re_\phi^{\frac{4}{5}}\left(\frac{r}{b}\right)^{\frac{12}{5}}. \tag{2.21}$$

It is of interest to note that, for both laminar and turbulent flow over the free disk, $Q_1$ depends on $r$ (in contrast to the Ekman layer on the disks in a rotating cavity, as discussed in §2.1). Thus the boundary layer entrains fluid from its (otherwise quiescent) surroundings; this is sometimes called the 'free disk pumping' effect.

### 2.3. *The Ekman layers in turbulent flow*

Equations (2.4) are valid in the core for turbulent flow, as well as for laminar flow. Hence $\bar{u} = 0$, and the Ekman-layer equations may be written

$$-2\Omega(v-\bar{v}) = \frac{1}{\rho}\frac{\partial \tau_r}{\partial z}, \quad 2\Omega u = \frac{1}{\rho}\frac{\partial \tau_\phi}{\partial z}. \tag{2.22}$$

For turbulent flow, it may be assumed that $u$ is given by (2.15) and, by analogy with (2.16), that

$$v = \begin{cases} \bar{v}(z/\delta^*)^{\frac{1}{7}}, & z \leqslant \delta^*, \\ \bar{v}, & z > \delta^*. \end{cases} \tag{2.23}$$

Integration of (2.22) with respect to $z$ from 0 to $\infty$ then gives

$$\frac{\tau_{r,0}}{\rho} = -\tfrac{1}{4}\Omega\bar{v}\delta^*, \quad \frac{\tau_{\phi,0}}{\rho} = -\tfrac{49}{60}\Omega u_1\,\delta^*. \tag{2.24}$$

By an argument analogous to that used by von Kármán to obtain the relations (2.19), it may be shown that

$$\left.\begin{aligned}\frac{\tau_{r,0}}{\rho} &= 0.0225\left(\frac{\nu}{\delta^*}\right)^{\frac{1}{4}} u_1(u_1^2+\bar{v}^2)^{\frac{3}{8}},\\ \frac{\tau_{\phi,0}}{\rho} &= 0.0225\left(\frac{\nu}{\delta^*}\right)^{\frac{1}{4}} \bar{v}(u_1^2+\bar{v}^2)^{\frac{3}{8}}.\end{aligned}\right\} \tag{2.25}$$

Equations (2.24) and (2.25) do not involve derivatives and can be solved to give

$$\frac{u_1}{\bar{v}} = -\frac{\sqrt{15}}{7} = -0.553,$$

and
$$\frac{\delta^*}{b} = 0.0983\, Re_\phi^{-\frac{1}{5}} \left(\frac{|\bar{v}|}{\Omega b}\right)^{\frac{3}{5}};$$

the minus sign in the expression for $u_1/\bar{v}$ is necessary to ensure that $\delta^*$ is positive. It follows that

$$\frac{Q_1}{\nu b} = -(\operatorname{sgn}\bar{v})\, 0.140\, Re_\phi^{\frac{4}{5}} \left(\frac{r}{b}\right)^{\frac{13}{5}} \left(\frac{|\bar{v}|}{\Omega r}\right)^{\frac{8}{5}} \tag{2.26}$$

and, when $Q_1 = \frac{1}{2}Q$,

$$\frac{\bar{v}}{\Omega r} = -(\operatorname{sgn} Q)\, 2.22\, |C_w|^{\frac{5}{8}} Re_\phi^{-\frac{1}{2}} \left(\frac{r}{b}\right)^{-\frac{13}{8}}. \tag{2.27}$$

## 3. The experimental apparatus

Before discussing the extended theory presented here, it is useful to describe the experiments, so that comparisons may be made during the course of the ensuing argument. Flow visualization and measurements of velocity using laser-Doppler anemometry (LDA) were made in three different rigs, which are described in §3.1, using a wide variety of optical instrumentation which is described in §3.2. Only the basic features of the rigs and instrumentation are presented here, and further details are given in the references cited.

### 3.1. *The rotating cavity rigs*

Each rig consisted of two disks of radius $b$, each disk being mounted on a central stainless-steel tube of bore $2a$ and surrounded by one of a series of perforated cylindrical shrouds (see figure 1*a*); the axial distance between the disks was $s$. In rig 3, a central driving shaft (diameter $\approx \frac{2}{3}a$) was fitted through the tubes. Details of the rigs, together with references where more detailed accounts are given, are summarized in table 1, and the shroud geometries (which were chosen to model certain engine configurations) are shown in table 2.

In each case, the whole assembly (that is, the two disks, the tubes, the shroud and, in rig 3, the driving shaft) was rotated at angular speed $\Omega$ using a variable-speed electric motor. Air was fed into the cavity, using a centrifugal blower, at volume flow rate $Q$, the value of $Q$ being measured by an Annubar differential-pressure sensing element or by rotameters. The maximum values of $\Omega$ and $Q$ which could be achieved for the different rigs are shown in table 1, together with the accuracy with which they could be determined.

All the rigs could be used for 'outflow' experiments in which the air was fed into the centre of the cavity through one of the tubes and removed through the shroud (only shrouds *A* and *D* were used for the outflow experiments in rig 3). In a few experiments in rig 1, a tubular gauze screen was inserted into the central tubes and rotated with them. The gauze ensured that the air entered the cavity with no axial component of velocity and with a radial component independent of position; these experiments are said to have a 'radial inlet'. The other outflow experiments, where no gauze was used, are referred to as having an 'axial inlet'.

Owing to leakage through the seals between the rotating and stationary components in rig 3, the measured flow rate had to be corrected, and the overall accuracy was thereby reduced. For this reason, only the experimental data for which the correction was less than 25 % of the corrected value of the flow rate are included in this paper.

In addition to the 'outflow' experiments, rig 3 was also used for 'inflow' experiments in which air entered the cavity through the shroud and was extracted

| | Rig 1 Owen & Pincombe (1980*a*) | Rig 2 Pincombe (1984) | Rig 3 Owen & Bilimoria (1977) |
|---|---|---|---|
| Disks | | | |
| Material | Perspex | Polycarbonate | Stainless steel |
| Outer radius, $b$ | 190 mm | 442.5 mm | 381 mm |
| Axial spacing, $s$ | 50.7 mm | 59 mm | 50.7 mm |
| Tube | | | |
| Bore, $2a$ | 38 mm | 88.6 mm | 76.2 mm |
| Rotation | | | |
| Max. angular speed, $\Omega_{max}$ | 2600 rev/min | 1000 rev/min | 1000 rev/min |
| Max. rotational Reynolds number, $Re_{\phi,max}$ | $6.5 \times 10^5$ | $1.3 \times 10^6$ | $10^6$ |
| Accuracy | Better than 1% | Better than 0.5% | Better than 0.5% |
| Flow rate | | | |
| Max. volume flow rate, $Q_{max}$ | 0.013 m³/s | 0.02 m³/s | 0.013 m³/s |
| Max. volume flow coefficient, $C_{w,max}$ | 4710 | 3000 | 2400 |
| Accuracy | Better than 3% | Better than 3% | Better than 3% |

TABLE 1. Data for the three rigs used (details of the shrouds are shown in table 2; $C_w$ and $Re_\phi$ are defined in (2.1) and (2.2))

through one of the central tubes. All six shrouds were used, and the swirl of the air at inlet varied from shroud to shroud. The shrouds with large perforations allowed air to enter the cavity with a tangential component of velocity significantly less than that of the shroud itself (shroud $E$ was the most extreme case of this). Smaller perforations had the effect of increasing the swirl of the air before it entered the cavity; in particular, air passing through the foam-filled slit in shroud $F$ entered with a tangential component of velocity virtually indistinguishable from that of the shroud itself.

### 3.2. *The optical instrumentation*

For the flow-visualization experiments, a Concept smoke generator, which produced clouds of oil particles whose diameter was approximately 0.5 μm, was used in conjunction with a 4 W argon-ion laser. Full details of the techniques involved are given by Owen & Pincombe (1980*b*).

For the LDA measurements in rigs 1 and 2, the optics were arranged in a forward-scatter real-fringe mode, with frequency shifting; for rig 3, a back-scatter mode was used, without frequency shifting. For rigs 1 and 3, the Doppler signal was processed using a tracking filter; this necessitated relatively high rates of seeding, and oil particles (generated from a Norgren 'micro-fog lubricator') were injected into the air before it entered the cavity. For rig 2, a photon-correlator was used to process the signal; although velocity measurements could, in principle, be accomplished in this case without 'artificial seeding', in practice oil particles (produced by the Concept generator) were introduced into the laboratory atmosphere.

In the absence of large velocity gradients (see Owen & Rogers 1975), the mean velocity could be measured by the tracking filter with an accuracy of approximately 1%. In an appraisal test of the photon-correlator (the measurements, which are not included in this paper, were made in rig 3), velocity measurements made by the tracking filter and by the photon-correlator were typically within 1% of each other.

Further details of the optical instrumentation are given by Pincombe (1984).

| | Material (thickness) | Number of holes | Angular spacing of holes | Axial position of holes | Hole size |
|---|---|---|---|---|---|
| Rig 1 | | | | | |
| 'Standard' shroud | Perspex (1 mm) | 30 | 12° | Mid-cavity | 12.7 mm diameter |
| 'Small-hole' shroud | Perspex (1 mm) | 30 | 12° | Mid-cavity | 3.2 mm diameter |
| 'Large-hole' shroud | Perspex (1 mm) | 30 | 12° | Mid-cavity | 25.4 mm diameter |
| Rig 2 | Polycarbonate (2 mm) | 32 | 11.25° | Mid-cavity | 32 mm diameter |
| Rig 3 | | | | | |
| Shroud *A* | Polycarbonate (1 mm) | 30 | 12° | Mid-cavity | 28.6 mm diameter |
| Shroud *B* | Polycarbonate (1 mm) | 60 | 6° | Alternately near the two disks | 20.6 mm diameter |
| Shroud *C* | Polycarbonate (1 mm) | 30 | 12° | Near one disk | 20.6 mm diameter |
| Shroud *D* | Polycarbonate (1 mm) | 30 | 12° | Mid-cavity | 6.4 mm diameter |
| Shroud *E* | Polycarbonate (1 mm) | Peripheral slot | Continuous | Mid-cavity | 11 mm width |
| Shroud *F* | Polycarbonate (1 mm) | Peripheral slot | Continuous | Mid-cavity | 5 mm width, foam filled |

TABLE 2. Data for the shrouds used with the three rigs

## 4. The flow structure

A schematic diagram of the flow structure is shown in figure 1 (*a*) for radial outflow and in figure 1 (*b*) for radial inflow; photographs of the flow in four cases of laminar outflow are shown in figure 2. The details of the photographic techniques have been described by Owen & Pincombe (1980*a*): each photograph shows the smoke pattern in an illuminated $(r, z)$-plane in rig 1; the white, smoke-filled areas contain air which has entered the cavity through the inlet at $r = a$ (that is, $x = 0.1$). It should also be remarked that the photographs show mirror images of the flow in the planes $z = 0$ and $z = s$, as well as the flow itself. Although figures 2 (*a*) and (*b*) were produced for the same flow conditions, figure 2 (*a*) was photographed within seconds of the smoke entering the cavity, whilst figure 2 (*b*) was photographed shortly after.

As first demonstrated by Hide (1968), these photographs confirm that, for laminar outflow, the flow is divided into four types of region, as indicated in figure 1 (*a*). Photographs of laminar inflow (not presented here) show the same four types of region (again confirming Hide's results). Further, visual observation revealed the same flow structure for turbulent flow (both outflow and inflow); this case was not considered by Hide. In all cases, there are

(i) a source region which distributes the fluid from the source to the Ekman layers (the term 'source layer', used by Hide and other authors, seems inappropriate since the region may occupy a substantial portion of the cavity);

(ii) Ekman layers on the disks, in which the volume flow rate is constant;

(iii) a sink layer which redistributes the flow from the Ekman layers into the sink; and

(iv) an interior core (showing dark in the photographs of figure 2) where the radial and axial components of velocity are zero and the tangential component is independent of $z$.

### 4.1. *The source region*

#### 4.1.1. *Radial outflow*

As explained in §3, two types of inlet were used in the experiments. The radial inlet gave a symmetrical flow structure in the source region, as shown in figures 1 (*a*), 2 (*a*) and 2 (*b*); for the axial inlet, the flow was asymmetrical about the axial plane $z = \frac{1}{2}s$, as shown in figures 2 (*c*) and (*d*).

The simplest model of boundary-layer flow inside the source region is that of the free disk described in §2.2. For the radial inlet, fluid from the source is entrained equally into the boundary layer on each disk, and, for $r < r_e$ (where $r_e$ is the radius at which these 'entrainment layers' turn into non-entraining Ekman layers), (2.14) for laminar flow or (2.21) for turbulent flow is assumed to be valid.

It is assumed that the entrainment layer persists until exactly half the incoming fluid has been entrained. Hence, when $r = r_e$, $Q_1 = \frac{1}{2}Q$. Writing, for convenience,

$$x = \frac{r}{b}, \quad x_e = \frac{r_e}{b}, \tag{4.1}$$

it follows that:

$$\left.\begin{aligned} x_e &= 0.424 C_w^{\frac{1}{2}} Re_\phi^{-\frac{1}{4}} \quad \text{for laminar flow;} \\ x_e &= 1.37 C_w^{\frac{4}{13}} Re_\phi^{-\frac{4}{13}} \quad \text{for turbulent flow.} \end{aligned}\right\} \tag{4.2}$$

The first of equations (4.2) agrees closely with the correlation obtained by Owen & Pincombe (1980*a*). The equation gives $x_e = 0.30$ when $C_w = 79$ and $R_{e\phi} = 2.5 \times 10^4$; this position is marked on figures 2 (*a*) and (*b*).

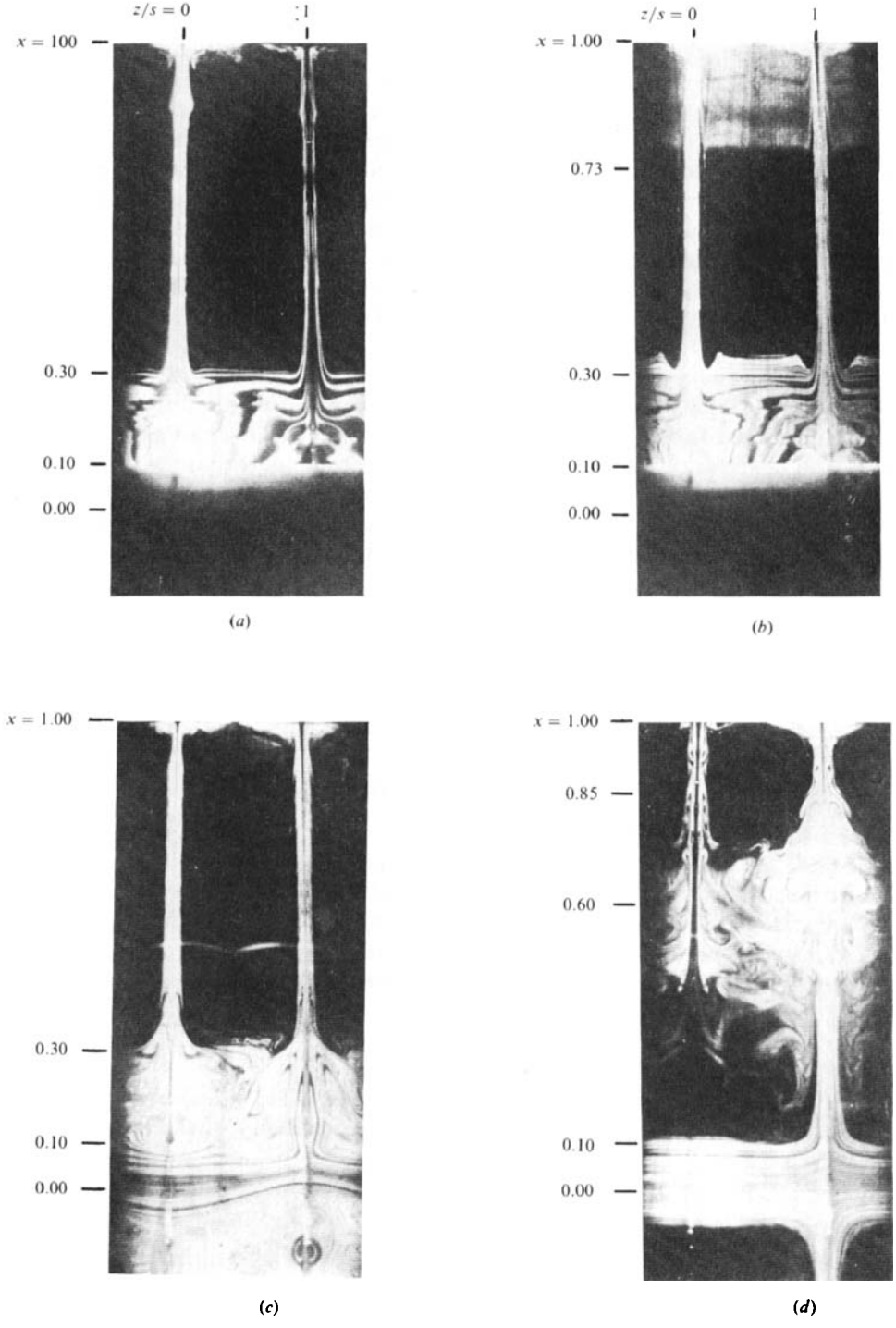


FIGURE 2. Flow visualization inside a rotating cavity ($G = 0.27$, $a/b = 0.10$, $Re_\phi = 2.5 \times 10^4$) with radial outflow. Radial inlet: (*a*) and (*b*) $C_w = 79$. Axial inlet: (*c*) $C_w = 79$; (*d*) $C_w = 314$.

Figure 2(*c*) shows the flow structure for the axial inlet case, where fluid enters the cavity through the centre of the upstream disk (the left-hand disk in the figure). For this flow rate and rotational speed ($C_w = 79$ and $Re_\phi = 2.5 \times 10^4$), vortex breakdown occurs and the central jet loses its axisymmetry. Fluid from the jet appears to be entrained equally by the two disks, and (4.2) provides a satisfactory estimate of the size of the source region: the value $x_e = 0.30$ is shown on figure 2(*c*).

Figure 2(*d*) shows the flow structure observed for the axial case with a higher flow rate ($C_w = 314$, $Re_\phi = 2.5 \times 10^4$) where the central jet impinges axisymmetrically onto the downstream disk. Flow visualization reveals that the smoke-filled fluid flows radially outward on the downstream disk, and smoke fills both the Ekman layers and the sink before it completely fills the source region. The interpretation (which is supported by the numerical solutions of Chew, Owen & Pincombe 1984) of this extreme case is that, after impinging on the downstream disk, the flow moves radially outwards as a wall jet. At a certain radius, some of the fluid detaches itself from the wall jet until, within a very small distance, exactly half of the original fluid has been disgorged from the downstream disk. This fluid flows radially inward and towards the upstream disk, where it is entrained into an entrainment layer (similar to the free-disk type that occurs with a radial inlet). It follows that, at the outer edge of the source region, the fluid has divided into two equal parts ready for entry into the Ekman layers, exactly as for a radial inlet, but the value of $x_e$ on the downstream disk is somewhat larger for an axial inlet.

An estimate of the radial extent of the source region near the downstream disk can be made by assuming that all (instead of half) the fluid is entrained by the downstream disk. The free-disk solutions, given in §2.2, are used for this estimate with $Q_1 = Q$. For the axial inlet case, (2.14) and (2.21) give:

$$\left.\begin{aligned} x_e &= 0.599 C_w^{\frac{1}{2}} Re_\phi^{-\frac{1}{4}} \quad \text{for the laminar case;} \\ x_e &= 1.79 C_w^{\frac{5}{13}} Re_\phi^{-\frac{4}{13}} \quad \text{for the turbulent case.} \end{aligned}\right\} \tag{4.3}$$

On the upstream disk (4.2) holds. Using the first of (4.2) for the upstream disk and that of (4.3) for the downstream disk, the corresponding values of $x_e$ for the two disks, with the data of figure 2(*d*), are 0.60 and 0.85; these positions are marked on figure 2(*d*). It was found that the second of (4.3) was in good agreement with the size of the source region measured using flow visualization on rig 2, which had an axial inlet; these experiments, which will be reported elsewhere, were conducted for $950 < C_w < 6600$ and $10^5 < Re_\phi < 1.3 \times 10^6$.

### 4.1.2. *Radial inflow*

The various shrouds (as described in §3), through which fluid enters the cavity, give different values of the tangential component of velocity of the incoming fluid. This is given by

$$\bar{v}_\phi / \Omega b = c,$$

where $c$ ($0 < c < 1$) is the 'swirl fraction', which may vary from shroud to shroud.

The model used for the flow in the cavity far from the disks, where angular momentum is conserved, is that of a free vortex. It follows that

$$\bar{v}_\phi / \Omega r = c x^{-2} \tag{4.4}$$

in the source region. Some of the fluid will be entrained into the boundary layers on the disks: the flow in these entrainment layers will have an outward component of velocity if $\bar{v}_\phi / \Omega r < 1$ and an inward component if $\bar{v}_\phi / \Omega r > 1$.

The entrainment can be quantified by assuming that (2.10) for laminar flow, or (2.26) for turbulent flow, gives a relationship between the volume flow rate through the layer and the tangential component of velocity outside the layer. Since $\bar{v}_\phi = \bar{v} + \Omega r$, it follows that

$$\frac{Q_1}{\nu b} = \pi Re_\phi^{\frac{1}{2}} (1 - cx^{-2}) \quad \text{for laminar flow,} \tag{4.5}$$

and

$$\frac{Q_1}{\nu b} = \operatorname{sgn}(1 - cx^{-2}) 0.293 \, |1 - cx^{-2}|^{\frac{8}{5}} Re_\phi^{\frac{4}{5}} x^{\frac{13}{5}} \quad \text{for turbulent flow.} \tag{4.6}$$

There is clearly a stagnation point on the disk, both for laminar and for turbulent flow, when $x = c^{\frac{1}{2}}$. For values of $x$ greater than this, there is outflow in the entrainment layers; for smaller values of $x$ there is inflow.

It is interesting to note that, by putting $c = 0$, this argument can be used when the flow outside the Ekman layer is quiescent. In this case, (4.5) and (4.6) give estimates for the flow entrained by the free disk with no imposed radial flow. For laminar flow, this 'linear Ekman layer' estimate is 1.16 times the value quoted in (2.14), which was found by Cochran (1934) using the full Navier–Stokes equations; the two values are surprisingly close.

It is further postulated that, as in the case of outflow, the source region extends from $r = b$ to $r = r_e$, where exactly half the incoming fluid has been entrained by each disk. Thus $Q_1 = \frac{1}{2}Q$ when $r = r_e$, and it follows that

$$x_e = \left[ c - \frac{1}{2\pi} |C_w| \, Re_\phi^{-\frac{1}{2}} \right]^{\frac{1}{2}} \quad \text{for laminar flow,} \tag{4.7}$$

and

$$x_e = [c - 2.22 \, |C_w|^{\frac{5}{8}} Re_\phi^{-\frac{1}{2}} x_e^{\frac{3}{2}}]^{\frac{1}{2}} \quad \text{for turbulent flow.} \tag{4.8}$$

The recirculation predicted for $x > c^{\frac{1}{2}}$ has been observed experimentally, and flow visualization has been used to estimate the size of the source region. Good agreement with the values of $x_e$ given by (4.7) and (4.8) was obtained using rig 3 with the six different shrouds described in §3 for a wide range of flow rates and rotational speeds ($C_w \leqslant 1800$, $5 \times 10^4 \leqslant Re_\phi \leqslant 10^6$). It was found that for shrouds *A*, *B*, *C* and *D* the appropriate value of $c$ was 0.54 for laminar flow and 0.59 for turbulent flow. For the foam-filled shroud *F*, which was designed to produce solid-body rotation at inlet, it was found that $c = 1$ gave a good correlation. For more details of these measurements, see Firouzian *et al.* (1985).

### 4.2. *The Ekman layers*

Owen & Pincombe (1980*a*) made detailed measurements of the radial and tangential components of velocity inside the Ekman layers for a rotating cavity with isothermal radial outflow. Using flow visualization, they observed long-wavelength ripples in the Ekman layer adjacent to the core region. These ripples had a wavelength approximately equal to $30D$, where $D$ is given by (2.8), and appeared to have a cellular structure; they were visible for

$$Re_r > 78 - \frac{32}{\pi} C_w \, Re_\phi^{-\frac{1}{2}} x^{-2}, \tag{4.9}$$

where the parameter $Re_r$ is the radial Reynolds number defined in (2.3). These instabilities, observed in outflow, appear to be related to the type II waves described

by Tatro & Mollo-Christensen (1967) for wavelengths between $23D$ and $33D$ which occurred, during radial inflow, when

$$Re_r > 56.3 - \frac{29.2}{\pi} C_w Re_\phi^{-\frac{1}{2}} x^{-2}. \tag{4.10}$$

Short-wavelength 'finger-like' disturbances were also observed by Owen & Pincombe: these propagated axially from the long-wavelength cells into the core when the critical value of $Re_r$ was exceeded by between 50 and 100%. The type I instabilities discussed by Tatro & Mollo-Christensen and also by Faller (1963) have a wavelength of approximately $12D$ and occur when

$$Re_r > 125 - \frac{1.83}{\pi} C_w Re_\phi^{-\frac{1}{2}} x^{-2}. \tag{4.11}$$

For $Re_r > 125$, these authors found that, for radial inflow, both types of wave were present, and the first manifestations of turbulence were bursts of high-frequency fluctuations.

For radial outflow with $Re_r > 200$, Owen & Pincombe observed that the tangential component of velocity measured in the core departed significantly from that predicted by the linear theory for laminar flow; this was taken to signal the onset of turbulent Ekman-layer flow. For the linear theory, the tangential component of velocity given by (2.11), for laminar flow, and (2.27), for turbulent flow, are equal when $Re_r \approx 180$. Although the nonlinear theory presented in this paper will give a slightly different value, $Re_r = 180$ gives a satisfactory criterion for transition from laminar to turbulent flow.

### 4.3. *The sink layer*

For most measurements presented in this paper, the radial thickness of the sink layer was significantly smaller (usually by at least an order of magnitude) than that of the source region. For laminar outflow, measurements of the size of the sink layer by Owen & Pincombe (1980*a*) were consistent with the theoretical estimate of Hide (1968). Owing to the relatively small thickness of the sink layer, no attempt has been made to correlate measurements for turbulent radial outflow nor for inflow, whether laminar or turbulent. For inflow, the sink layer was always limited to the region $x < 0.15$.

A phenomenon observed during the radial-outflow experiments on rig 1 was that of fluid 'ingress' through the shroud at $x = 1$. This is demonstrated in figure 2(*b*) where there is a white smoke-filled region near the sink layer. Above a certain rotational speed, which depended on the flow rate and on the hole size in the shroud, there was evidence that external fluid was entrained into the cavity through the holes in the shroud, despite the fact that the net flow was radially outward. This ingress phenomenon has been reported for rotor–stator systems (see Bayley & Owen 1970; Phadke & Owen 1983) but never, as far as the present authors are aware, for a rotating cavity with radial outflow.

Flow-visualization tests showed that (as in the rotor–stator case) the 'critical' speed, beyond which ingress occurred, was proportional to the flow rate and decreased with increasing hole size. For the small-hole, standard-hole and large-hole shrouds with rig 1, ingress was observed for $Re_\phi/C_w > 1100$, 110 and 50 respectively, over a range of $Re_\phi$ up to $3 \times 10^5$. For rig 3, ingress was observed, in some experiments, for $Re_\phi/C_w > 440$.

The ingress of external fluid is attributed to the fact that, at a sufficiently high rotational speed, the pressure level inside the cavity may become sub-atmospheric. Thus ingress can occur even when there is a superimposed outflow of fluid. It is not known whether the ingress is confined to some holes in the shroud while egress occurs at others, or whether ingress and egress occur simultaneously at the same hole.

Referring to figure 2(*a*), the outer sink layer is clearly visible; in figure 2(*b*) (which was photographed shortly after figure 2*a*) the ingress extends to $x = 0.76$. Photographs taken at later times reveal that the 'ingress region' does not extend inwards beyond this. It is interesting to compare the radial extent of the ingress region for radial outflow with the source region for radial inflow discussed above. In the limiting case of zero inflow, with the swirl fraction $c = 0.54$, (4.7) gives $x_e = 0.73$; this suggests that the ingress region for radial outflow is similar to the source region for radial inflow.

Under certain conditions, the ingressive fluid can significantly affect the flow structure throughout the cavity. This was observed when the large-hole shroud was used in rig 1: when ingress occurred at the same time as vortex breakdown in the inlet jet at the centre, the axisymmetry of the flow was disrupted, the Ekman layers disappeared and the inlet jet precessed violently about the axis of rotation.

### 4.4. *The effect of buoyancy*

When both disks are symmetrically heated to a temperature greater than that of the incoming fluid, the flow structure is similar to that for isothermal flow. For high rotational speeds, when gravitational effects are insignificant, the only modification necessary to the theory presented in this paper is the inclusion of the effect of variable density and viscosity, together with an energy equation. Work on the heat-transfer problem is well advanced and will be reported elsewhere.

When one disk only is heated, there is an 'axial wind' in the core from the hot disk to the cold disk. The effect of this is to make $Q_1$ dependent on $r$, even in the Ekman layers; the theory must therefore involve a matching of the boundary layers on the two disks through the core region which lies between them. Work on this problem is well advanced.

The other effect of buoyancy which needs to be mentioned is that, for radial outflow when the disks are differentially heated, flow near the hot disk can be destabilized.

## 5. The nonlinear equations of motion

### 5.1. *The basic equations*

The discussion in §4.2 of the boundary layers (outside the source and sink regions) on the disks of the rotating cavity was in terms of the non-entraining Ekman layers described by the linear theory of §§2.1 and 2.3. When the nonlinear inertial and centrifugal terms are included in the equations of motion, it is not strictly proper to retain the term 'Ekman layer' since, by definition, Ekman layers occur only when the nonlinear terms are negligible. However, the non-entraining boundary layers which occur in practice are so similar to Ekman layers that, in this paper, the term 'Ekman layer' is retained even in the nonlinear case. It will be seen later that, even when individual nonlinear terms are not negligible, there tends to be a self-cancelling effect so that departure from the Ekman solution is quite small: this gives *a posteriori* support to the usage described. (The term 'boundary layer' is used throughout as a generic term to include both the 'nonlinear Ekman layer' and the 'entrainment layer' in the source region.)

The equations of continuity and momentum in the boundary layers on the disks, referred to axes rotating with the cavity, are (when $\bar{u} = 0$):

$$\frac{1}{r}\frac{\partial}{\partial r}(ru)+\frac{\partial w}{\partial z}=0; \tag{5.1}$$

$$u\frac{\partial u}{\partial r}+w\frac{\partial u}{\partial z}-\frac{v^2-\bar{v}^2}{r}-2\Omega(v-\bar{v})=\frac{1}{\rho}\frac{\partial \tau_r}{\partial z}; \tag{5.2}$$

$$u\frac{\partial v}{\partial r}+w\frac{\partial v}{\partial z}+\frac{uv}{r}+2\Omega u=\frac{1}{\rho}\frac{\partial \tau_\phi}{\partial z}; \tag{5.3}$$

together with the boundary conditions (for the disk $z = 0$):

$$\left.\begin{aligned} u=v=w=0 \quad &\text{when } z=0;\\ u\to 0, \quad v\to\bar{v} \quad &\text{when } z\to\infty. \end{aligned}\right\} \tag{5.4}$$

(It may be noticed that (2.22) are approximations to (5.2) and (5.3).)

It is useful to rewrite (5.2) and (5.3), using (5.1), as

$$\frac{1}{r}\frac{\partial}{\partial r}(ru^2)+\frac{\partial}{\partial z}(uw)-\frac{v^2-\bar{v}^2}{r}-2\Omega(v-\bar{v})=\frac{1}{\rho}\frac{\partial \tau_r}{\partial z}, \tag{5.5}$$

$$\frac{1}{r^2}\frac{\partial}{\partial r}(r^2uv)+\frac{\partial}{\partial z}(vw)+2\Omega u=\frac{1}{\rho}\frac{\partial \tau_\phi}{\partial z}. \tag{5.6}$$

It is next assumed that (see §§2.2, 2.3)

$$u = u_1 f(z/\delta^*), \tag{5.7}$$

and

$$v = \bar{v}[1-g(z/\delta^*)], \tag{5.8}$$

where $u_1, \bar{v}, \delta^*$ are, as yet, unknown functions of $r$; the functions $f(\eta)$, $g(\eta)$, where

$$\eta = z/\delta^*, \tag{5.9}$$

must be specified. The theory will be developed for general functions $f(\eta)$, $g(\eta)$ subject to the conditions

$$f(0)=0, \quad g(0)=1, \quad f(\eta)\to 0, \quad g(\eta)\to 0 \quad \text{as } \eta\to\infty, \tag{5.10}$$

so that the conditions on $u$ and $v$ in (5.4) are automatically satisfied. For comparison with experiment, particular forms of $f$ and $g$ are used, as described below.

For laminar flow, by analogy with the Ekman-layer solutions given in (2.7),

$$f(\eta) = e^{-\pi\eta}\sin(\pi\eta), \quad g(\eta) = e^{-\pi\eta}\cos(\pi\eta). \tag{5.11}$$

For turbulent flow, a generalization of (2.15) and (2.16) is used of the form

$$\left.\begin{aligned} f(\eta)&=\eta^{1/n}(1-\eta), \quad g(\eta)=1-\eta^{1/n}, \quad \eta\leqslant 1,\\ f(\eta)&=g(\eta)=0, \quad \eta>1. \end{aligned}\right\} \tag{5.12}$$

It is usual to follow von Kármán and to take $n = 7$ (and this will be done in the comparisons below), but several authors have suggested that the different values of $n$ are appropriate for different Reynolds-number ranges (see, for example, Schlichting 1978).

Once the functions $f(\eta)$, $g(\eta)$ have been specified, (5.5) and (5.6) may be integrated to give

$$I_2\frac{1}{r}\frac{\mathrm{d}}{\mathrm{d}r}(ru_1^2\delta^*)+(2I_4-I_5)\frac{\bar{v}^2}{r}+2I_4\Omega\bar{v}=-\frac{1}{\rho}\tau_{r,0}, \tag{5.13}$$

and
$$(I_1-I_3)\frac{1}{r^2}\frac{\mathrm{d}}{\mathrm{d}r}(r^2u_1\bar{v}\delta^*)+2\Omega I_1 u_1 = -\frac{1}{\rho}\tau_{\phi,0}, \tag{5.14}$$

where
$$\left.\begin{aligned} I_1 &= \int_0^\infty f(\eta)\,\mathrm{d}\eta, \\ I_2 &= \int_0^\infty f^2(\eta)\,\mathrm{d}\eta, \\ I_3 &= \int_0^\infty f(\eta)\,g(\eta)\,\mathrm{d}\eta, \\ I_4 &= \int_0^\infty g(\eta)\,\mathrm{d}\eta, \\ I_5 &= \int_0^\infty g^2(\eta)\,\mathrm{d}\eta. \end{aligned}\right\} \tag{5.15}$$

The values of $I_1$, $I_2$, $I_3$, $I_4$, $I_5$ for the special cases defined in (5.11) and (5.12) are shown in table 3.

The local volume flow rate is given by
$$Q_1 = 2\pi I_1 r u_1 \delta^*, \tag{5.16}$$

and it is convenient to write (5.13) and (5.14) using $Q_1$ instead of $u_1$ as one of the dependent variables. They become
$$\frac{1}{r}\frac{\mathrm{d}}{\mathrm{d}r}\left(\frac{Q_1^2}{r\delta^*}\right)+\frac{4\pi^2 I_1^2(2I(2I_4-I_5)}{I_2}\frac{\bar{v}^2}{r}+\frac{8\pi^2 I_1^2 I_4}{I_2}\Omega\bar{v} = -\frac{4\pi^2 I_1^2}{I_2}\frac{1}{\rho}\tau_{r,0}, \tag{5.17}$$

$$\frac{1}{r^2}\frac{\mathrm{d}}{\mathrm{d}r}(\bar{v}rQ_1)+\frac{I_1}{I_1-I_3}\Omega\frac{Q_1}{r\delta^*} = -\frac{2\pi I_1}{I_1-I_3}\frac{1}{\rho}\tau_{\phi,0}. \tag{5.18}$$

For laminar flow, the values of $\tau_{r,0}$ and $\tau_{\phi,0}$ are given by
$$\frac{1}{\rho}\tau_{r,0} = \frac{\mu}{\rho}\left.\frac{\partial u}{\partial z}\right|_{z=0} = \frac{\nu f''(0)}{2\pi I_1}\frac{Q_1}{r\delta^{*2}}, \tag{5.19}$$

$$\frac{1}{\rho}\tau_{\phi,0} = \frac{\mu}{\rho}\left.\frac{\partial v}{\partial z}\right|_{z=0} = -\nu g'(0)\frac{\bar{v}}{\delta^*}. \tag{5.20}$$

For turbulent flow, relations similar to (2.25) may be found in the form
$$\left.\begin{aligned} \frac{\tau_{r,0}}{\rho} &= K_n^2\left(\frac{\nu}{\delta^*}\right)^{2/(n+1)} u_1(u_1^2+\bar{v}^2)^{(n-1)/2(n+1)}, \\ \frac{\tau_{\phi,0}}{\rho} &= K_n^2\left(\frac{\nu}{\delta^*}\right)^{2/(n+1)} \bar{v}(u_1^2+\bar{v}^2)^{(n-1)/2(n+1)}, \end{aligned}\right\} \tag{5.21}$$

where the coefficients $K_n^2$ for $n = 5, 6, 7, 8, 9$ are given in table 4. (The value of $K_1^2$ shown in the table is discussed below; its value is given in (5.35).) In terms of the new dependent variable $Q_1$, these expressions become
$$\left.\begin{aligned} \frac{\tau_{r,0}}{\rho} &= K_n^2\left(\frac{\nu}{\delta^*}\right)^{2/(n+1)} \frac{Q_1}{2\pi I_1 r\delta^*}\left[\frac{Q_1^2}{4\pi^2 I_1^2 r^2\delta^{*2}}+\bar{v}^2\right]^{(n-1)/2(n+1)}, \\ \frac{\tau_{\phi,0}}{\rho} &= K_n^2\left(\frac{\nu}{\delta^*}\right)^{2/(n+1)} \bar{v}\left[\frac{Q_1^2}{4\pi^2 I_1^2 r^2\delta^{*2}}+\bar{v}^2\right]^{(n-1)/2(n+1)}. \end{aligned}\right\} \tag{5.22}$$

| | Laminar flow | Turbulent flow | |
|---|---|---|---|
| | | $1/n$ power law | $n = 7$ |
| $I_1$ | $\frac{1}{2}\pi$ | $n^2/(n+1)(2n+1)$ | 0.408 |
| $I_2$ | $\frac{1}{8}\pi$ | $n^3/(n+1)(n+2)(3n+2)$ | 0.207 |
| $I_3$ | $\frac{1}{8}\pi$ | $3n^2/2(n+1)(n+2)(2n+1)$ | 0.0681 |
| $I_4$ | $\frac{1}{2}\pi$ | $1/(n+1)$ | 0.125 |
| $I_5$ | $\frac{3}{8}\pi$ | $2/(n+1)(n+2)$ | 0.0278 |

TABLE 3. Values of the coefficients defined in (5.15)

| $n$ | 1 | 5 | 6 | 7 | 8 | 9 |
|---|---|---|---|---|---|---|
| $K_n^2$ | $\pi$ | 0.0384 | 0.0290 | 0.0225 | 0.0179 | 0.0145 |
| $K_n$ | $\sqrt{\pi}$ | 0.196 | 0.170 | 0.150 | 0.134 | 0.120 |
| $P_n$ | $\pi$ | 0.200 | 0.176 | 0.159 | 0.145 | 0.133 |
| $P'_n$ | $\frac{1}{2}\pi$ | 1.58 | 1.90 | 2.22 | 2.55 | 2.90 |
| $p$ | 2 | 1.67 | 1.64 | 1.63 | 1.61 | 1.60 |

TABLE 4. Values of various parameters for six values of $n$.
The values for $n = 1$ correspond to laminar flow

At this stage, there are two equations, (5.17) and (5.18), for the three unknown quantities $Q_1$, $\bar{v}$ and $\delta^*$. If any one of the three quantities is known, the other two can be calculated. In practice, either $\bar{v}$ or $Q_1$ is usually known or can be assumed.

If the distribution of $\bar{v}$ is known (for example, $\bar{v}/\Omega r = -1$ for the free disk or $\bar{v}/\Omega r = cx^{-2}$ for a free vortex), then $Q_1$ and $\delta^*$ can be computed. In this way, more general estimates of the size of the source region may be found than those obtained from the linear equations discussed in §4.1. A number of such computations has been made, but the results are not presented here: they are more important when buoyancy effects are significant.

If the value of $Q_1$ is known, as is the case for the Ekman layers on the disks (where $Q_1 = \frac{1}{2}Q$), then (5.17) and (5.18) can be used to calculate $\bar{v}$ and $\delta^*$. It is this case that will be developed in the next section.

### 5.2. *The non-dimensional form*

At this stage, $Q_1$ is taken to be a function of $r$ (although, in the Ekman layers, $Q_1$ is constant); this will enable the equations to be used for the entrainment layers if alternative assumptions are made for the flow in the source region.

It is convenient to define a parameter

$$p = \frac{3n+5}{2(n+1)}, \tag{5.23}$$

where $n = 1$ for laminar flow and $1/n$ is the exponent of $\eta$ used in (5.12) for turbulent flow. Composite parameters $\lambda$, $\lambda_0$ are defined as

$$\lambda = \operatorname{sgn}(Q_1)\, P'_n \left|\frac{2Q_1}{\nu b}\right|^{p-1} Re_\phi^{-\frac{1}{2}}, \tag{5.24}$$

$$\lambda_0 = \operatorname{sgn}(Q_1)\, P'_n\, |C_w|^{p-1} Re_\phi^{-\frac{1}{2}}, \tag{5.25}$$

where, for laminar flow,

$$P_1' = \left[ -\frac{f'(0)}{64\pi^4 I_1 I_4 [g'(0)]^3} \right]^{\frac{1}{4}}, \tag{5.26}$$

and, for turbulent flow,

$$P_n' = \frac{1}{(64\pi^4 I_1 I_4)^{\frac{1}{4}} K_n} \left[ \frac{16\pi^2 I_1^2 I_4}{I_1 + I_4} \right]^{1-\frac{1}{4}p}. \tag{5.27}$$

The values of $P_n'$ for $n = 1, 5, 6, 7, 8, 9$ are given in table 4.

Application of the method described (for the special case of turbulent flow with $n = 7$) to solve the linear equations (2.22) gives, for both laminar and turbulent flow,

$$V_{\text{lin}} = -\lambda_0 x^{-p}, \tag{5.28}$$

$$\frac{\delta^*_{\text{lin}}}{b} = P_n \left| \frac{2Q_1}{\nu b} \right|^{2-p} Re_\phi^{-\frac{1}{4}} x^{p-2}, \tag{5.29}$$

where the subscript lin is used to indicate the solution of the linear equations, and

$$V = \bar{v}/\Omega r. \tag{5.30}$$

For laminar flow, the coefficient in (5.29) is

$$P_1 = \left[ -\frac{f'(0) g'(0)}{4 I_1 I_4} \right]^{\frac{1}{4}} \tag{5.31}$$

and, for turbulent flow,

$$P_n = \left[ \frac{I_1 + I_4}{16\pi^2 I_1^2 I_4} \right]^{1-\frac{1}{4}p} \frac{K_n}{(4 I_1 I_4)^{\frac{1}{4}}}. \tag{5.32}$$

The numerical values of $P_n$ for $n = 1, 5, 6, 7, 8, 9$ are given in table 4. For ease of computation, it is worth noting that, for turbulent flow,

$$4\pi (I_1 I_4)^{\frac{1}{4}} P_n P_n' = 1. \tag{5.33}$$

Providing $f'(0) = -g'(0)$ for laminar flow, (5.26), (5.31) reduce to (5.27), (5.32) respectively (with $n = 1$) as long as

$$K_1^2 = |f'(0)| = |g'(0)|. \tag{5.34}$$

The value of $K_1$ given in table 4 is obtained from this equation.

The non-dimensional boundary-layer thickness is defined in terms of the linear solution as

$$\delta = \delta^*/\delta^*_{\text{lin}}. \tag{5.35}$$

Then (5.17) and (5.18), which have $Q_1, \bar{v}$ and $\delta^*$ as dependent variables and $r$ as the independent variable, become

$$\frac{x}{\delta}\frac{\mathrm{d}\delta}{\mathrm{d}x} = A_1 \frac{x}{\lambda}\frac{\mathrm{d}\lambda}{\mathrm{d}x} + A_2 + A_3 \frac{x^p \Psi}{\lambda\delta} + (A_4 V^2 + A_5 V) \frac{x^{2p}\delta^2}{\lambda^2}, \tag{5.36}$$

$$\frac{x}{V}\frac{\mathrm{d}V}{\mathrm{d}x} = A_7 \frac{x}{\lambda}\frac{\mathrm{d}\lambda}{\mathrm{d}x} + A_8 + \frac{A_9}{V} + A_{10} \frac{x^p \Psi}{\lambda\delta}, \tag{5.37}$$

where

$$\Psi = \left[ \frac{I_1}{I_1 + I_4} \left( \frac{x^{2p} V^2 \delta^2}{\lambda^2} - 1 \right) + 1 \right]^{2-p}, \tag{5.38}$$

and the coefficients $A_j$ are tabulated in table 5. (The coefficient $A_6$ has been reserved for use when buoyancy effects are included.) It is of interest to note that, for the linear

| $j$ | $A_j$ | Laminar flow | Turbulent flow | |
|---|---|---|---|---|
| | | | $1/n$ power law | $n = 7$ |
| 1 | $p/(p-1)$ | 2 | $(3n+5)/(n+3)$ | 2.6 |
| 2 | $-(p-1)$ | $-1$ | $-(n+3)/2(n+1)$ | $-0.625$ |
| 3 | $2I_1/I_2$ | 8 | $2(n+2)(3n+2)/n(2n+1)$ | 3.94 |
| 4 | $I_1(2I_4-I_5)/I_2I_4$ | 5 | $2(n+1)(3n+2)/n(2n+1)$ | 3.50 |
| 5 | $2I_1/I_2$ | 8 | $2(n+2)(3n+2)/n(2n+1)$ | 3.94 |
| 7 | $I_3/(p-1)(I_1-I_3)$ | $\frac{1}{3}$ | $6(n+1)/(n+3)(2n+1)$ | 0.32 |
| 8 | $-2$ | $-2$ | $-2$ | $-2.0$ |
| 9 | $-2I_1/(I_1-I_3)$ | $-\frac{8}{3}$ | $-4(n+2)/(2n+1)$ | $-2.4$ |
| 10 | $-2I_1/(I_1-I_3)$ | $-\frac{8}{3}$ | $-4(n+2)/(2n+1)$ | $-2.4$ |

TABLE 5. Coefficients in (5.36) and (5.37)

equations, the only terms remaining in (5.36) and (5.37) are those involving the coefficients $A_3$, $A_5$, $A_9$ and $A_{10}$.

In the Ekman layers, where $Q_1 = \frac{1}{2}Q$, it is convenient to define the new independent variable

$$\xi = x^p/\lambda_0. \tag{5.39}$$

Noting that $\mathrm{d}\lambda/\mathrm{d}x = 0$ and $\lambda = \lambda_0$ in these layers, (5.36) to (5.38) become

$$\frac{\mathrm{d}\delta}{\mathrm{d}\xi} = \frac{1}{p}\left[A_2\frac{\delta}{\xi} + A_3\Psi + (A_4V^2 + A_5V)\xi\delta^3\right], \tag{5.40}$$

$$\frac{\mathrm{d}V}{\mathrm{d}\xi} = \frac{1}{p}\left[(A_8V + A_9)\frac{1}{\xi} + A_{10}V\frac{\Psi}{\delta}\right], \tag{5.41}$$

where

$$\Psi = \left[\frac{I_1}{I_1+I_4}(\xi^2V^2\delta^2 - 1) + 1\right]^{2-p}. \tag{5.42}$$

These equations are in a form suitable for numerical integration (using, for example, a Runga–Kutta technique) as long as suitable initial values are chosen.

### 5.3. *Initial values*

#### 5.3.1. *Radial outflow*

If the model described in §4.1.1 is used for the source region, the starting value of $\xi$ is easily derived from either (4.2) or (4.3). The corresponding initial value of $\delta$ is given by (2.14) or (2.20), and the initial value of $V$ is $-1$ (since the model takes $v_\phi = 0$). These values are given in table 6.

It is of interest, however, to investigate the effect of different starting and initial conditions, and the results are shown in figures 3 and 4 for both laminar and turbulent flow. It might well be expected that Ekman-layer-type flow begins within the source region, starting at values of $\xi$ much less than those given in table 6. (It will be demonstrated in §6 that such starting values of $\xi$ are suitable for predicting the tangential component of velocity.) It appears from figures 3 and 4 that, for a wide range of starting conditions, the dependence of $V$ on $\xi$ gives a 'universal' curve; the 'universal' curves for laminar flow and turbulent flow are, of course, slightly different.

It is remarkable that all the solutions depart very little from the linear curves, even when the individual inertial and centrifugal terms are quite large. Rogers & Owen

| | Laminar flow | | Turbulent flow | |
|---|---|---|---|---|
| | $\xi$ | $\delta$ | $\xi$ | $\delta$ |
| Both disks, radial inlet<br>Upstream disk, axial inlet | 1.12 | 1.59 | 0.755 | 4.51 |
| Downstream disk, axial inlet | 2.26 | 1.59 | 1.16 | 5.85 |

TABLE 6. Possible starting values of $\xi$ and $\delta$ for radial outflow

(1983) have investigated the relative size of all the terms in the equations, and they show that the nonlinear terms tend to be self-cancelling. This means that the linear theory (that is, the true Ekman layer) is a good approximation for a much wider range of conditions than would be expected.

It is possible that, in an experiment, a laminar entraining boundary layer may develop into a turbulent Ekman layer or that a turbulent entrainment layer may develop into a laminar Ekman layer. If this occurs, the simple universal relationships are not valid, and the matching of the Ekman layer to the entrainment layer must be carried out separately for each set of experimental data.

Transition from laminar to turbulent flow may also occur within the 'free disk' boundary layer. The relevant parameter is the local rotational Reynolds number $Re$ (where $Re = \Omega r^2/\nu$); it is generally accepted that flow in the boundary layer will be turbulent for $Re \gtrsim 3 \times 10^5$. Further, transition from turbulent to laminar flow may occur within the Ekman layer. This transition is associated with the radial Reynolds number $Re_r$; whilst there is no generally accepted value, it has been shown in §4.2 that the flow in an Ekman layer is turbulent for $Re_r \gtrsim 180$. It is therefore possible for an entrainment layer to start with laminar flow (at small radii), to become turbulent and then develop into an Ekman layer which could begin by being turbulent and then become laminar! In fact, there is a variety of possible combinations of laminar and turbulent flow in the two layers on each disk. For simplicity, the computations have been carried out only for those cases where transition does not occur within the Ekman layer.

### 5.3.2. *Radial inflow*

For inflow, the initial value of $\xi$ can vary considerably from experiment to experiment, depending on the values of $C_w$ and $Re_\phi$. It may happen that the largest value of $|\xi|$ (which occurs near the peripheral inlet) in one experiment is less than the smallest value (near the central outlet) in another experiment. There can, therefore, be no 'universal' curves (like those found in the outflow case), and each set of experimental data must be treated separately.

The simplest model is to start the computation at the stagnation point where $x = c^{\frac{1}{2}}$ with $V = 0$ (that is, $v_\phi = \Omega r$). It is not obvious what initial value of $\delta$ should be used, but test computations have shown that the solution is not sensitive to the value chosen for $\delta_I$.

## 6. Comparison with experiments

In figures 5–11 a comparison is made between the theory discussed in §5 and the experimental values of the tangential component of velocity, obtained in the rigs described in §3. For convenience, subscripts L and T are used to indicate laminar

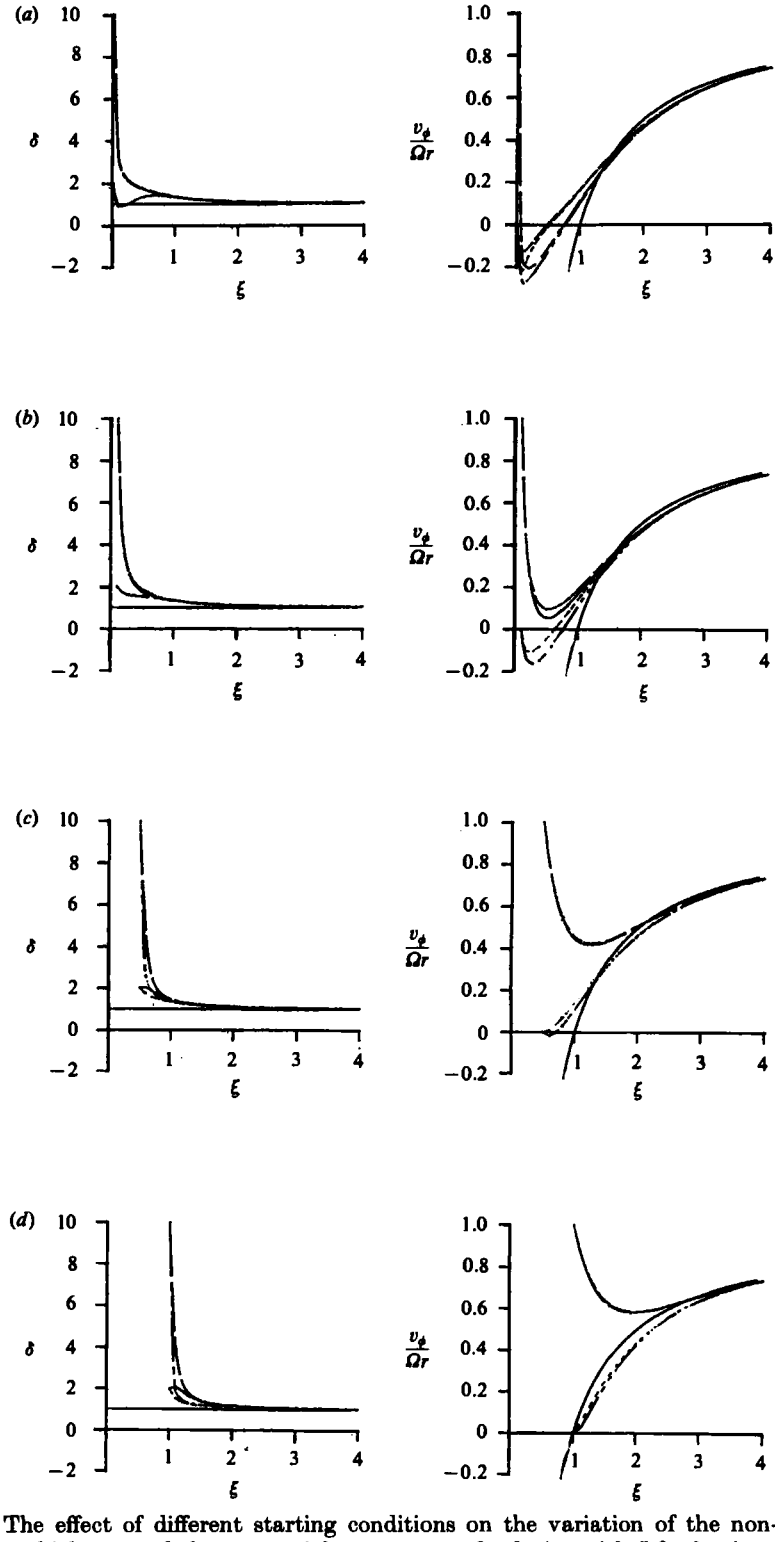


FIGURE 3. The effect of different starting conditions on the variation of the non-dimensional Ekman-layer thickness and the tangential component of velocity with $\xi$ for laminar outflow. (*a*) $\xi_I = 0.01$, (*b*) $\xi_I = 0.1$, (*c*) $\xi_I = 0.5$, (*d*) $\xi_I = 1.0$. ---, $\delta_I = 2$, $v_{\phi,I}/\Omega r = 1$; - - -, 2, 0; ———, 10, 1; ——- -—, 10, 0; ——, linear theory ($\delta = 1$, $v_\phi/\Omega r = 1 - 1/\xi$).

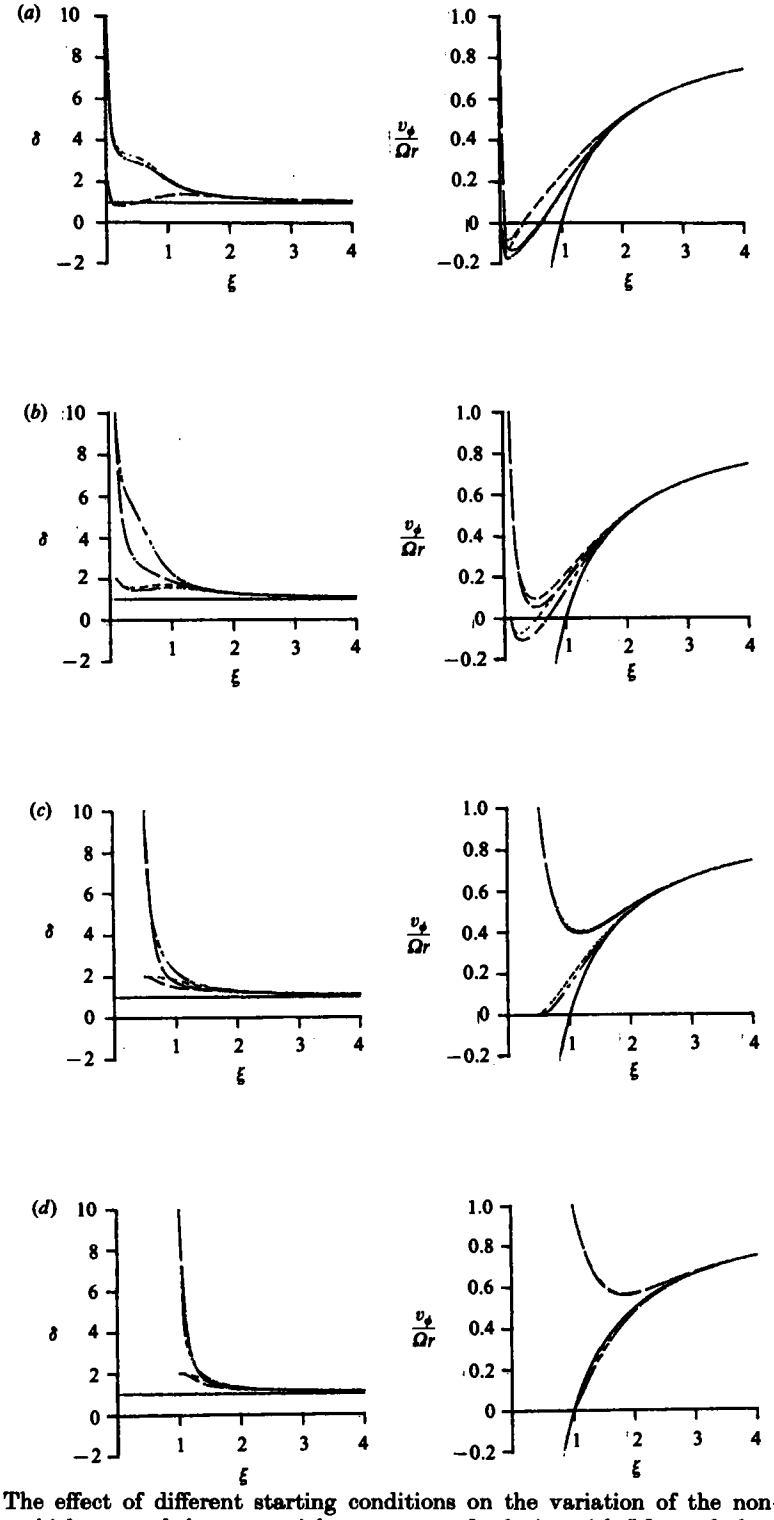


FIGURE 4. The effect of different starting conditions on the variation of the non-dimensional Ekman-layer thickness and the tangential component of velocity with $\xi$ for turbulent outflow. (*a*) $\xi_I = 0.01$, (*b*) $\xi_I = 0.1$, (*c*) $\xi_I = 0.5$, (*d*) $\xi_I = 1.0$. – – –, $\delta_I = 2$, $v_{\phi,I}/\Omega r = 1$; - - -, 2, 0; ———, 10, 1; — - - —, 10, 0; ——, linear theory ($\delta = 1$, $v_\phi/\Omega r = 1 - 1/\xi$).

and turbulent values, the subscript e is used to denote the quantities in table 6 (with the addition of a prime, where necessary, to indicate values for the downstream disk with an axial inlet), and the subscript I is used for starting and initial values. In each diagram, the theoretical curves corresponding to the linear theories of §§2.1 and 2.3 are also shown. The measurements were made in or near the mid-axial plane ($z = \frac{1}{2}s$).

### 6.1. *Radial outflow*

For the theoretical curves in figures 5 to 8, various starting conditions were used. When $\xi_I = \xi_e$, it is consistent to take $\delta_I = \delta_e$. When the computation is started well within the source region, it can be assumed that the Ekman layer is very large initially; a convenient value to take for $\delta_I^*$ is $\frac{1}{2}s$ and, for all the experiments reported here, this means that $\delta_I$ lies between 3 and 30. The results of the computations are insensitive to the value of $\delta_I$ within the range 1 to 100, and so (with the exception of one curve in each of figures 5*a* and 5*b*) all the curves shown here have been computed with $\delta_I = 15$.

Figures 5(*a*) and (*b*) show the variation of $v_\phi/\Omega r$ with $\xi$ when the experimental values of $Re_r$ were less than and greater than 180, respectively. Those points which were (according to the criteria given in §4.3) subject to the effects of ingress have been omitted from the figures. For laminar flow, the experimental data ranged over the conditions $s/b = 0.133$ and 0.267, $170 < C_w < 970$, $2.5 \times 10^4 < Re_\phi < 8.1 \times 10^5$, $0.40 < x < 0.98$. For turbulent flow, the corresponding conditions were $s/b = 0.133$ and 0.267, $690 < C_w < 2500$, $2.5 \times 10^4 < Re_\phi < 1.2 \times 10^6$, $0.60 < x < 0.98$. Data points arising from experiments with radial and axial inlets are shown by separate symbols. Also shown are the theoretical linear and nonlinear curves; the latter have starting values $\xi_I = \xi_e$, 0.1 and 0.5 (together with the appropriate values of $\delta_I$, and $v_{\phi,I} = 0$).

Superficial inspection of the graphs reveals that there is broad agreement between the theoretical curves and the experimental data (including many of the data that lie within the source region). Most of the scatter occurs in the data from rig 3 (which was prone to leakage), and is greater for turbulent flow than for laminar flow.

For laminar flow, figure 5(*a*) shows that the nonlinear curves for which $\xi_I \leqslant 0.5$ merge with each other before $v_\phi/\Omega r \approx 0.1$ ($\xi \approx 1$); they merge with the curve having $\xi_I = \xi_e$ when $v_\phi/\Omega r \approx 0.5$ ($\xi \approx 2$) and with the linear curve when $v_\phi/\Omega r \approx 0.9$ ($\xi \approx 10$). For turbulent flow, all three nonlinear curves merge with each other and with the linear curve when $v_\phi/\Omega r \approx 0.4$ ($\xi \approx 1.7$). It may be noted that, in both diagrams, data points for which $v_\phi/\Omega r \leqslant 0.1$ are in the source region. For the lower values of $\xi$ shown, there is good agreement between the nonlinear curves and, despite the scatter, the experimental data for both laminar and turbulent flow. Further, it can be seen that many of the points in the source region also lie on the nonlinear curves (except for the laminar curve with $\xi_I = \xi_e$); for this reason, the theoretical curves for the remaining outflow diagrams have been started with $\xi_I = 0.1$. For the larger values of $\xi$ shown, the experimental data are consistently below the theoretical curves, though only slightly below in the laminar case. The difference between the average of the measured values and the theoretical curves in turbulent flow appears to be a maximum when $\xi \approx 2$ ($v_\phi/\Omega r \approx 0.5$); at this point the average error in $v_\phi/\Omega r$ is approximately 7% of the theoretical value.

Bearing in mind that three rigs were used over a wide range of conditions, it appears that $\xi_L$ and $\xi_T$ can act as universal parameters for laminar and turbulent flow respectively.

Figure 6 shows the variation of $v_\phi/\Omega r$ with $C_w$, at (*a*) $x = 0.633$ and (*b*) $x = 0.833$

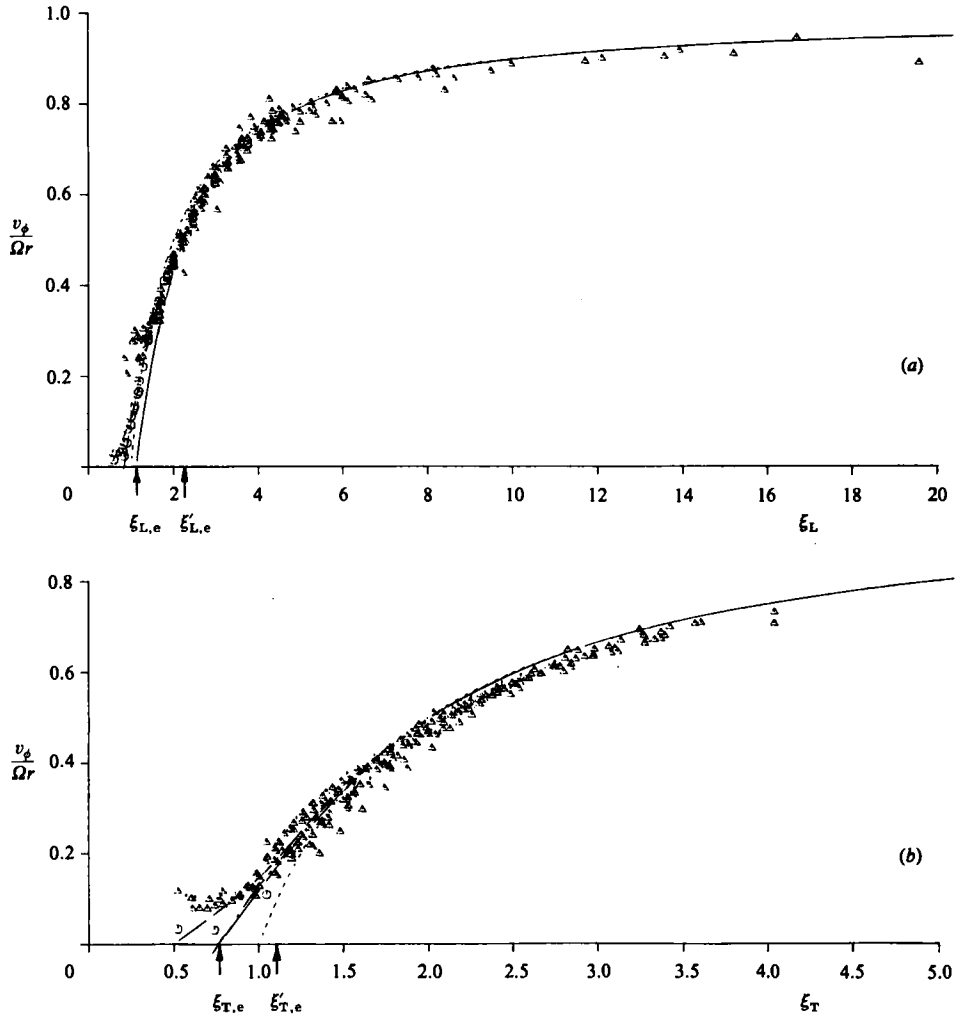


FIGURE 5. Variation of tangential component of velocity with the non-dimensional variable $\xi$ for outflow. (*a*) $Re_r < 180$, laminar theory; (*b*) $Re_r > 180$, turbulent theory: - - -, linear theory; ——, nonlinear theory ($\xi_I = \xi_e, \delta_I = \delta_e, V_{\phi,I} = 0$); – – –, nonlinear theory ($\xi_I = 0.5, \delta_I = 15, V_{\phi,I} = 0$); – - –, nonlinear theory ($\xi_I = 0.1, \delta_I = 15, V_{\phi,I} = 0$). Experimental data: ○, radial inlet; △, axial inlet.

in rig 2 ($s/b = 0.133$), for three values of $Re_\phi$. It should be noted that all the data in figures 6 to 8 (with the exception of one set of data in figure 8*a*) were obtained using an axial inlet.

In figures 6(*a*) and (*b*), the intercepts between the linear laminar and turbulent curves occur where $C_w = 716$ and 942 respectively; in both cases, the intercept corresponds to $Re_r = 180$. For both graphs, agreement between the experimental data and the nonlinear curves is, in the main, good. The data obtained with $x = 0.633$ and $Re_\phi = 10^5$, in which the theoretical curves tend to zero and the experimental data remain positive, are the exception to this agreement: no satisfactory explanation has yet been found for this. It is worth noting that, in the source region of rig 2, $v_\phi/\Omega r \geqslant 0.1$; measured values of $v_\phi$ were always positive.

Figure 7 shows the variation of $v_\phi/\Omega r$ with $Re_\phi$ for (*a*) three values of $C_w$ for which

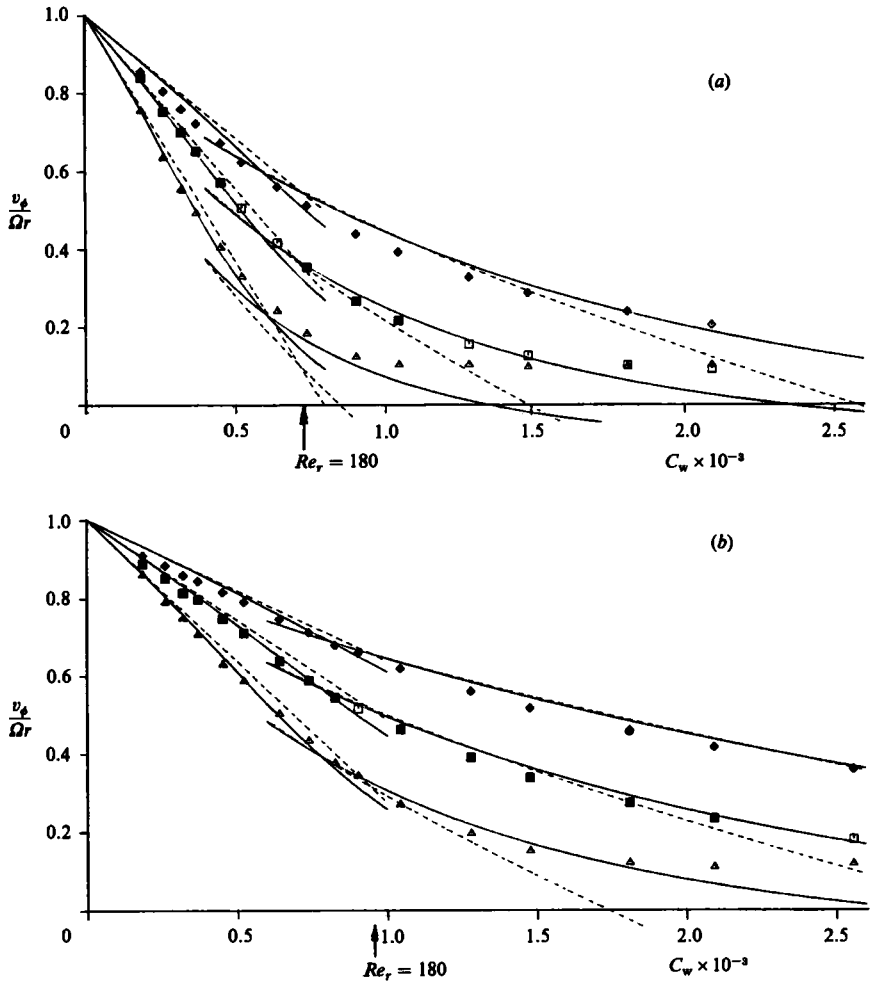


FIGURE 6. Variation of tangential component of velocity with flow rate for outflow. (*a*) $x = 0.633$; (*b*) 0.833. - - -, linear theory; ——, nonlinear theory. Experimental data: ▲, $Re_\phi = 10^5$; ■, $2 \times 10^5$; ◆, $4 \times 10^5$. Hollow symbols are in the source region.

$Re_r < 180$ and (*b*) three values of $C_w$ for which $Re_r > 180$. The data for $C_w = 1414$ and 2500 were obtained using rig 2, and the other data were obtained in rig 3.

In figure 7(*a*), the measured velocities are, apart from those at the highest rotational speeds, in good agreement with the nonlinear curves. The fact that the measured values for $Re_\phi > 0.8 \times 10^6$ are lower than the theoretical curves is believed to be related to the presence of ingress into the sink layer. From figure 7(*b*), it can be seen that the divergence between the linear and nonlinear theoretical curves is greater than for the laminar results in figure 7(*a*). For $C_w = 1414$ and 2500, the agreement between the measured velocities and the nonlinear curves is good; the reason for the disagreement when $C_w = 940$ (in rig 3) is not understood.

Figure 8 shows the radial variation of $v_\phi/\Omega r$ for (*a*) laminar flow with $Re_\phi = 5 \times 10^4$ and (*b*) turbulent flow with $C_w = 2500$. Referring to figure 8(*a*), the tests for $C_w = 253$ and 487 were conducted with an axial inlet; the tests for $C_w = 689$ were conducted with a radial inlet. The source region is, as expected, smaller in the latter case; as

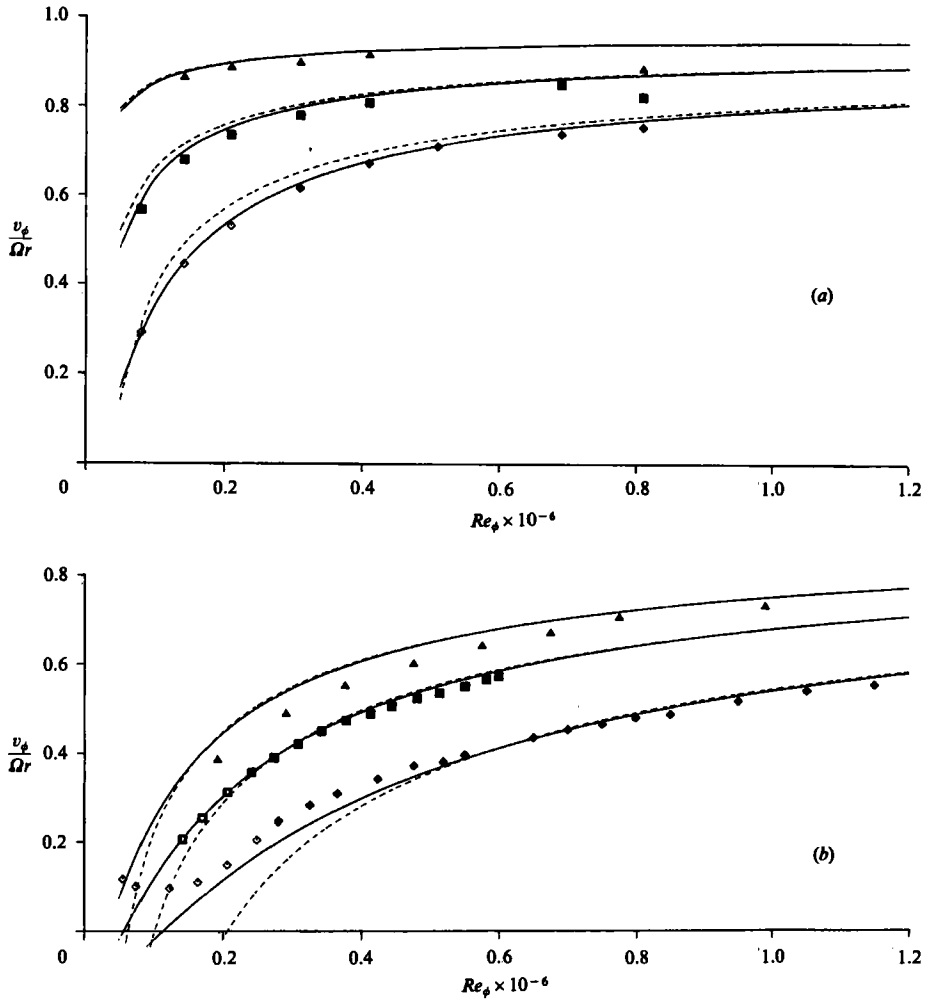


FIGURE 7. Variation of tangential component of velocity with rotational speed for outflow ($x = 0.767$). (*a*) $Re_r < 180$, laminar theory; (*b*) $Re_r > 180$, turbulent theory: - - -, linear theory; ——, nonlinear theory. Experimental data: ▲, (*a*) $C_w = 170$; (*b*) 940; ■, (*a*) 396; (*b*) 1414; ◆, (*a*) 710; (*b*) 2500. Hollow symbols are in source region.

a consequence, the experimental data are in good agreement with the nonlinear curve over a wider range than is the case for the axial inlet data. Referring to figure 8(*b*), the experimental data tend to be higher than the nonlinear curves for $v_\phi/\Omega r < 0.4$ ($\xi < 1.7$) and sightly lower for $v_\phi/\Omega r > 0.4$.

### 6.2. *Radial inflow*

The starting value of $x$ for the computations for radial inflow are given by $x_I = c^{\frac{1}{2}}$, where $c$ is the swirl fraction described in §4.1.2. For shroud $A$, the size of the source region was found to be in good agreement with the predictions described in that section if $c = 0.54$ for laminar flow and $c = 0.59$ for turbulent flow. However, better agreement for the distribution of the tangential component of velocity is obtained by taking $c = 0.59$ for this shroud for both laminar and turbulent flow; this gives $x_I = 0.77$. For the foam-filled shroud $F$, where the incoming fluid was given

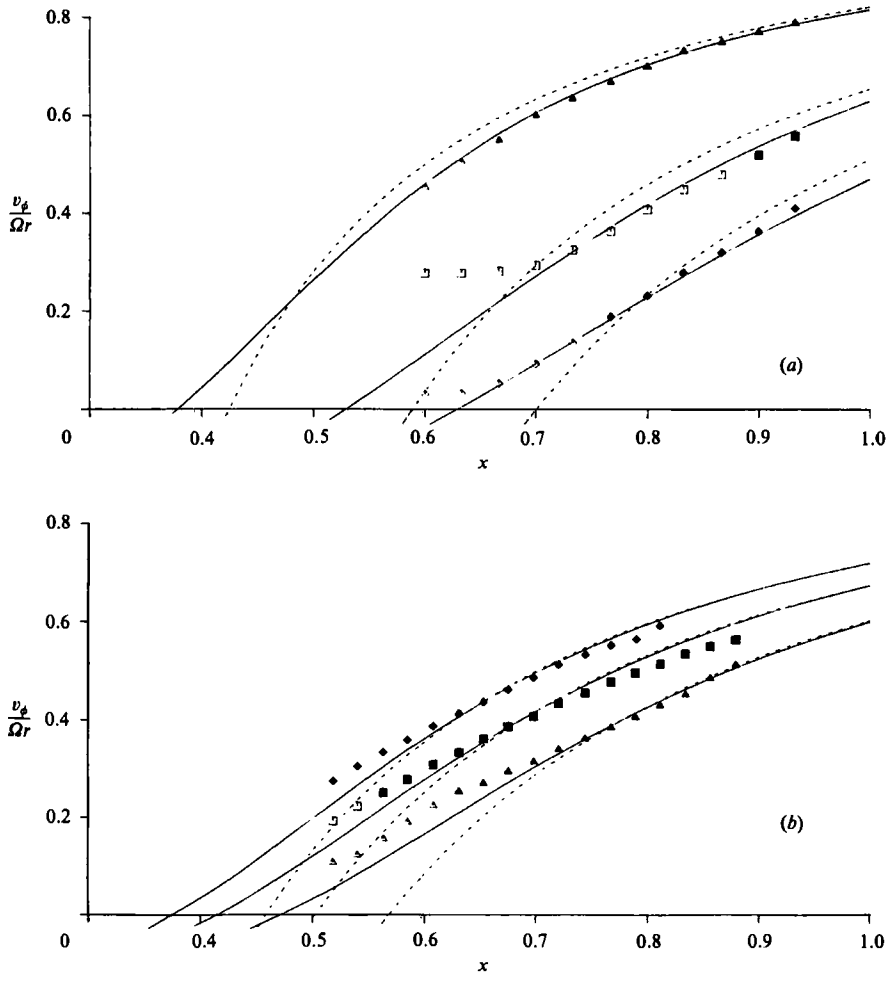


FIGURE 8. Variation of tangential component of velocity with radius for outflow. (*a*) $Re_r < 180$, $Re_\phi = 5 \times 10^4$, laminar theory; (*b*) $Re_r > 180$, $C_w = 2500$, turbulent theory: - - -, linear theory; ——, nonlinear theory. Experimental data: ▲, (*a*) $C_w = 253$, (*b*) $Re_\phi = 5.47 \times 10^5$; ■, (*a*) $C_w = 487$, (*b*) $Re_\phi = 8.17 \times 10^5$; ◆, (*a*) $C_w = 689$, (*b*) $Re_\phi = 1.1 \times 10^6$. Hollow symbols are in source region.

'solid-body' rotation, $c$ was taken to be unity; this gives $x_I = 1$. (Although not presented here, results for shroud $E$, with its wide slot at inlet, were also computed. For this shroud it is to be expected that the swirl fraction would be much smaller, and $c = 0.4$ gave fair agreement with experiments.)

Assuming, as in the outflow case, that $\delta_I^* = \frac{1}{2}s$, the value of $\delta_I$ lies between 3.5 and 31; computations carried out for values between 1 and 100 showed negligible variation in the theoretical curves. For all the computations discussed below, values of $\delta_I = 15$ and $v_{\phi,I}/\Omega r = 1$ were used.

Figures 9 to 11 show comparisons between the measured and computed tangential components of velocity, inside the interior core between the Ekman layers, for radial inflow in rig 3. Nearly 300 velocity measurements were made for $s/b = 0.133$, $170 < |C_w| < 1800$, $2.9 \times 10^4 < Re_\phi < 8 \times 10^5$, $0.28 < x < 0.93$. The data presented in these figures were chosen to illustrate the salient features of the flow and to show typical comparisons between the theoretical and experimental results. As explained

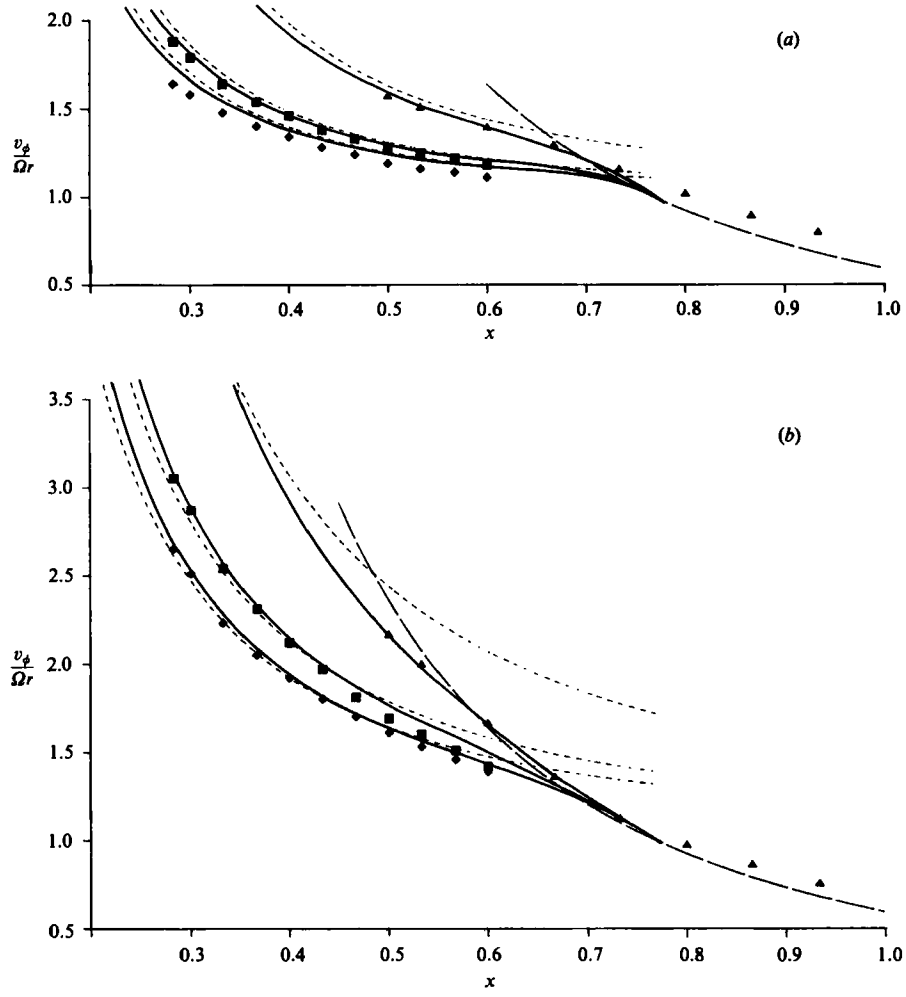


FIGURE 9. Variation of tangential component of velocity with radius for inflow (shroud $A$). ($a$) $Re_r < 180$, laminar theory; ($b$) $Re_r > 180$, turbulent theory: ---, linear theory; ——, nonlinear theory; – – –, free vortex. Experimental data: ▲, ($a$) $C_w = -440$, $Re_\phi = 1.97 \times 10^5$; ($b$) $-1415$, $1.97 \times 10^5$; ■, ($a$) $-309$, $4 \times 10^5$; ($b$) $-946$, $4 \times 10^5$; ◆, ($a$) $-309$, $6 \times 10^5$; ($b$) $-946$, $6 \times 10^5$.

in §5.3.2, the results of the computations depend strongly on starting values of $\xi$; for this reason, although $\xi$ is a useful variable for the computations, it cannot be thought of as a universal parameter, and no curves are presented for $v_\phi/\Omega r$ as a function of $\xi$.

Figure 9 shows the radial variation of $v_\phi/\Omega r$ for ($a$) laminar flow and ($b$) turbulent flow. The measurements were made using the shroud $A$; the curves shown are those obtained by the linear theory of §2, the nonlinear theory of §5 (with the starting conditions discussed above) and, for $x > x_e$, the free-vortex distribution given in (4.4) with $c = 0.59$. It should be noted that the intercepts between the latter curve and the linear curve mark the approximate position of the limit, $x = x_e$, of the source region.

Referring to figure 9($a$), the nonlinear curves diverge from each other for $x < 0.77$ and are, except for the results for $Re_\phi = 6 \times 10^5$, in good agreement with the measured velocities. In the main, the linear curves overestimate, and the free-vortex curve

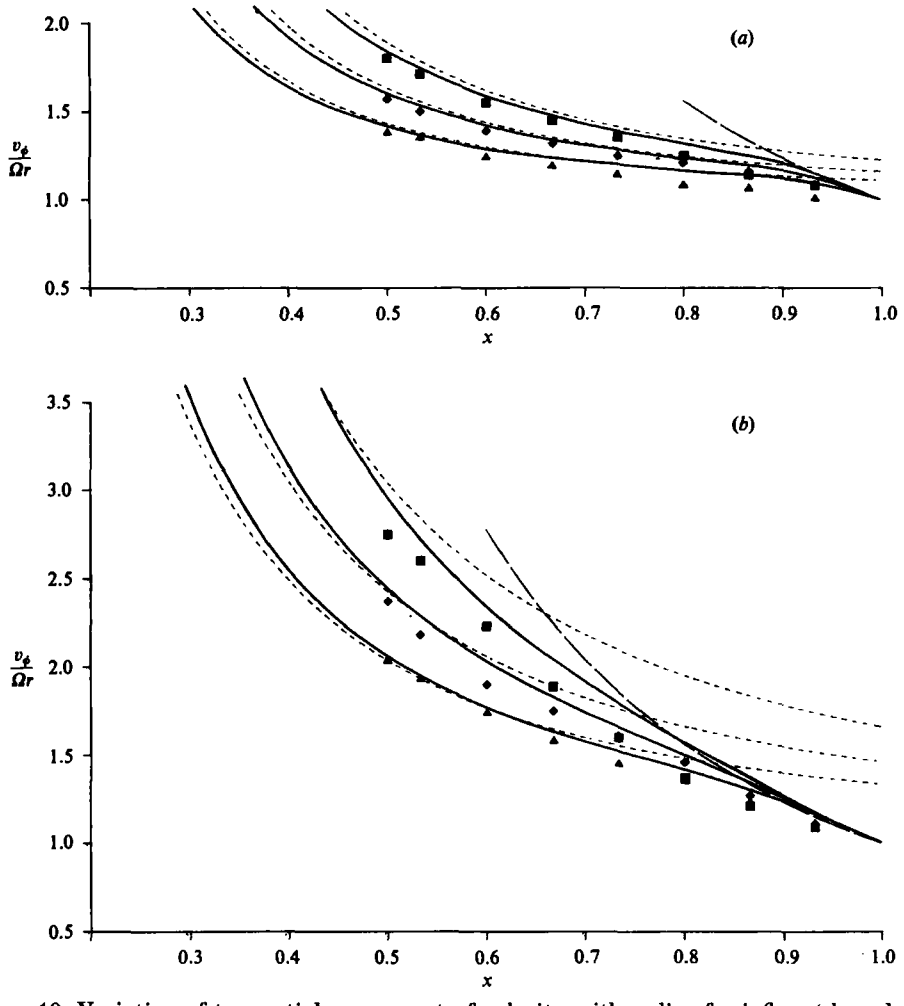


FIGURE 10. Variation of tangential component of velocity with radius for inflow (shroud $F$). ($a$) $Re_r < 180$, laminar theory; ($b$) $Re_r > 180$, turbulent theory: ---, linear theory; ——, nonlinear theory; – – –, free vortex. Experimental data: ■, ($a$) $C_w = -440$, $Re_\phi = 9.85 \times 10^4$; ($b$) $-1425$, $9.85 \times 10^4$; ◆ ($a$) $-440$, $1.97 \times 10^5$; ($b$) $-1396$, $1.97 \times 10^5$; ▲, ($a$) $-399$, $3.45 \times 10^5$; ($b$) $-1310$, $3.45 \times 10^5$.

underestimates, the measured values. It is clear that a larger value of the swirl fraction $c$ would produce better agreement for $x_I < x < 1$, and this would have little effect on the nonlinear Ekman-layer curves. Similar comments apply to figure 9($b$), where the agreement between the nonlinear turbulent curves and the measured velocities is, for most tests, better than for the laminar case.

Figure 10 also shows the radial variation of $v_\phi/\Omega r$ for ($a$) laminar and ($b$) turbulent flow. Here measurements were made using shroud $F$, and the theoretical curves using $c = 1$. Referring to figure 10($a$), the linear curves overestimate the experimental data, but the agreement between the nonlinear curves and the data is good, particularly at the smaller values of $x$. Similar comments apply to figure 10($b$), but the agreement between the nonlinear turbulent curves and the measured velocities is not as good as it was for shroud $A$.

Figure 11 shows the variation of $v_\phi/\Omega r$ (at $x = 0.467$ and using shroud $A$) with ($a$)

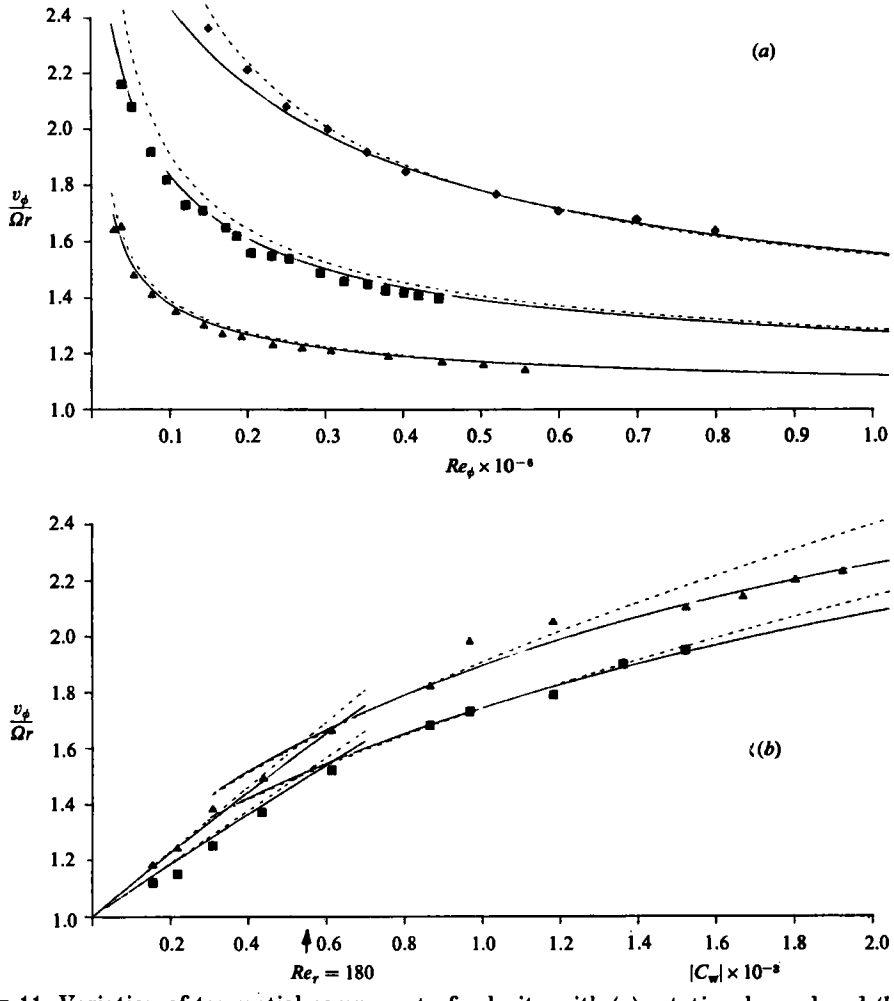


FIGURE 11. Variation of tangential component of velocity with (*a*) rotational speed and (*b*) flow rate for inflow (shroud $A$, $x = 0.467$): - - -, linear theory; ——, nonlinear theory. Experimental data: ▲, (*a*) $C_w = -170$; (*b*) $Re_\phi = 4 \times 10^5$; ■, (*a*) $C_w = -396$; (*b*) $Re_\phi = 6 \times 10^5$; ◆, (*a*) $C_w = -946$.

$Re_\phi$, for $|C_w| = 170$, 396 and 946, and with (*b*) $|C_w|$, for $Re_\phi = 4 \times 10^5$ and $6 \times 10^5$. Referring to figure 11 (*a*), the agreement between the nonlinear laminar theory and the experimental measurements for $|C_w| = 170$ and 396 (where $Re_r < 180$), is very good. The agreement between the nonlinear turbulent theory and the experimental velocities for $|C_w| = 946$ (where $Re_r > 180$) is also very good (apart from two measurements at the smaller value of $Re_\phi$).

Referring to figure 11 (*b*), the intercept between the linear laminar and turbulent curves occurs at $|C_w| = 528$ ($Re_r = 180$). For the smaller values of $|C_w|$, the measured velocities are in good agreement with the nonlinear laminar curves; for the larger values of $|C_w|$, the measured velocities (with the exception of two measurements at $Re_\phi = 4 \times 10^5$) are in good agreement with the nonlinear turbulent curves. As for the outflow results, it would appear that $Re_r = 180$ can be regarded as a reasonable criterion for transition from laminar to turbulent flow.

## 7. Conclusions

Models for the flow in the source region have been presented, and the radial extent of the region predicted, for a rotating cavity with either a radial outflow or a radial inflow of fluid. For radial outflow, it is assumed that the boundary layer in the source region is similar to that on a rotating 'free disk'; for radial inflow, a free vortex is postulated outside the boundary layer. The size of the source region is estimated in both cases by assuming that the entrainment layer becomes an Ekman layer when exactly half the incoming fluid has been entrained by each disk in the cavity; good agreement was found with the experimental measurements.

Both linear and nonlinear theories for the Ekman layers have been developed using integral-momentum techniques. The predictions of the tangential component of velocity outside the Ekman layers have been tested against extensive velocity measurements made, using laser-Doppler anemometry, inside three different experimental rigs. Tests were conducted over a wide range of operating conditions, and of inlet conditions, with either radial outflow or radial inflow of air imposed on the rotating system.

For the radial-outflow case, the experimental measurements confirmed that there were universal relationships between the non-dimensional tangential component of velocity $v_\phi/\Omega r$ and the variables $\xi_L$ and $\xi_T$; these variables are special cases of the variable $\xi$ defined in (5.39), with $p = 1$ for laminar flow and $p$ given by (5.23) for turbulent flow. Transition from laminar to turbulent flow in the Ekman layers occurred at, or near, the intercept of the laminar and turbulent linear curves when $Q/2\pi\nu r \approx 180$. For laminar radial outflow, the linear curves were in good agreement with the experimental data for $3 < \xi_L < 20$; the nonlinear curves were in good agreement with the data for the entire experimental range $0.1 < \xi_L < 20$. For turbulent radial outflow, the linear curves were in reasonable agreement with the data for $1.5 < \xi_T < 4$; the nonlinear curves were in reasonable agreement with the data for $1 < \xi_T < 4$ (no data were available for $\xi_T > 4$).

For radial inflow, there were no universal relationships between $v_\phi/\Omega r$ and $\xi_L$ or $\xi_T$, and the results (both theoretical and experimental) depend heavily on conditions at the inlet. The nonlinear computations, for both laminar and turbulent flow, were begun inside the source region where $r/b = c^{\frac{1}{2}}$ (where $c$ is an empirically determined swirl fraction) at a point where there was a stagnation point on the disk, and the initial value of $v_\phi/\Omega r$ was unity. As for the radial-outflow case, transition from laminar to turbulent flow occurred when $|Q|/2\pi\nu r \approx 180$. The laminar linear curves tended to overestimate the velocities, particularly at the larger values of $r/b$ (near the source region); the nonlinear laminar and turbulent curves were, in the main, in good agreement with the experimental data.

The extension of the methods used in this paper to the important case of non-isothermal flow involves allowing for the dependence of density and viscosity on temperature, together with discussion of an integral energy equation. In this case too, it is necessary to use the theory, in the way described in §5, to determine the flow within the boundary layers in the source region. A preliminary account of this work (together with more details of some of the work presented in this paper) is given in Owen & Rogers (1983), Rogers & Owen (1983), and Pincombe, Owen & Rogers (1983). Further work on the problem of heat transfer is in progress, and it is hoped to report on this in the near future.

The authors wish to thank Rolls-Royce Limited, Motoren- und Turbinen-Union and the Science and Engineering Research Council for sponsoring much of the work described in this paper. They are also indebted to Mr M. Firouzian for his assistance with the velocity measurements for radial inflow.

## REFERENCES

BARCILON, V. 1970 Some inertial modifications of the linear viscous theory of steady rotating fluid flows. *Phys. Fluids* **13**, 537.

BAYLEY, F. J. & OWEN, J. M. 1970 The fluid dynamics of a shrouded disk system with a radial outflow of coolant. *J. Engng Power* **92**, 335.

BENNETTS, D. A. & HOCKING, L. M. 1973 On nonlinear Ekman and Stewartson layers in a rotating fluid. *Proc. R. Soc. Lond.* A **333**, 469.

BENNETTS, D. A. & JACKSON, W. D. N. 1974 Source–sink flow in a rotating annulus: a combined laboratory and numerical study. *J. Fluid Mech.* **66**, 689.

CHEW, J. W., OWEN, J. M. & PINCOMBE, J. R. 1984 Numerical predictions for laminar source sink flow in a rotating cylindrical cavity. *J. Fluid Mech.* **143**, 451.

COCHRAN, W. G. 1934 The flow due to a rotating disc. *Proc. Camb. Phil. Soc.* **30**, 365.

DORFMAN, L. A. 1963 *Hydrodynamic Resistance and the Heat Loss of Rotating Solids.* Edinburgh: Oliver and Boyd.

FALLER, A. J. 1963 An experimental study of the instability of the laminar Ekman boundary layer. *J. Fluid Mech.* **15**, 560.

FIROUZIAN, M., OWEN, J. M., PINCOMBE, J. R. & ROGERS, R. H. 1985 Flow and heat transfer in a rotating cylindrical cavity with a radial inflow of fluid. Parts I and II. *Intl J. Heat and Fluid Flow.* To be published.

GREENSPAN, H. P. 1968 *The Theory of Rotating Fluids.* Cambridge University Press.

HIDE, R. 1968 On source–sink flows in a rotating fluid. *J. Fluid Mech.* **32**, 737.

KÁRMÁN, TH. VON 1921 Über laminare und turbulente Reibung. *Z. angew. Math. Mech.* **1**, 233.

OWEN, J. M. & BILIMORIA, E. D. 1977 Heat transfer in rotating cylindrical cavities. *J. Mech. Engng Sci.* **19**, 175.

OWEN, J. M. & PINCOMBE, J. R. 1980*a* Velocity measurements inside a rotating cylindrical cavity with a radial outflow of fluid. *J. Fluid Mech.* **99**, 111.

OWEN, J. M. & PINCOMBE, J. R. 1980*b* The use of optical techniques in the interpretation of heat transfer measurements. *AGARD Conf. Proc.* **281**, 15–1.

OWEN, J. M. & ROGERS, R. H. 1975 Velocity biasing in laser doppler anemometers. In *Proc. Intl Symposium on Laser Doppler Anemometry* (LDA-75), 89.

OWEN, J. M. & ROGERS, R. H. 1983 Solution of the integral momentum equations for an Ekman layer in a heated rotating cavity. 1. The full equations and the linear approximation. *Rep. No.* 80/TFMRC/15a, *School of Engng and Appl. Sciences, University of Sussex.*

PHADKE, U. P. & OWEN, J. M. 1983 An investigation of ingress for an 'air-cooled' shrouded rotating disk system with radial-clearance seals. *J. Engng Power* **105**, 178.

PINCOMBE, J. R. 1984 Optical measurements of the flow in a rotating cylinder. D.Phil. thesis, University of Sussex.

PINCOMBE, J. R., OWEN, J. M. & ROGERS, R. H. 1983 Solution of the integral momentum equations for an Ekman layer in a heated rotating cavity. 3. Comparison between theory and experiment. *Rep. No.* 82/TFMRC/17a, *School of Engng and Appl. Sciences, University of Sussex.*

ROGERS, R. H. & OWEN, J. M. 1983 Solution of the integral momentum equations for an Ekman layer in a heated rotating cavity. 2. The nondimensional form of the equations and the numerical solution. *Rep. No.* 81/TFMRC/16a, *School of Engng and Appl. Sciences, University of Sussex.*

SCHLICHTING, H. 1978 *Boundary-Layer Theory.* New York: McGraw-Hill.

TATRO, P. R. & MOLLO-CHRISTENSEN, E. L. 1967 Experiments on Ekman layer stability. *J. Fluid Mech.* **28**, 531.